

New physics in double Higgs production at NLO

Bo-Yan Huang^{a)}

Physics Department, University of Illinois at Chicago.

(Dated: 29 June 2021)

After observing the Higgs boson by the ATLAS and CMS experiments at the LHC, accurate measurements of its properties, which allow us to study the electroweak symmetry breaking mechanism, become a high priority for particle physics. The most promising of extracting the Higgs self-coupling at hadron colliders is by examining the double Higgs production, especially in the $b\bar{b}\gamma\gamma$ channel. In this work, we presented full loop calculation for both SM and New Physics effects of the Higgs pair production to next-to-leading-order (NLO), including loop-induced processes $gg \rightarrow HH$, $gg \rightarrow HHg$, and $qg \rightarrow qHH$. We also included the calculation of the corrections from diagrams with only one QCD coupling in $qg \rightarrow qHH$, which was neglected in the previous studies. With the latest observed limit on the HH production cross-section, we studied the constraints on the effective Higgs couplings for the LHC at center-of-mass energies of 14 TeV and a provisional 100 TeV proton collider within the Future-Circular-Collider (FCC) project. To obtain results better than using total cross-section alone, we focused on the $b\bar{b}\gamma\gamma$ channel and divided the differential cross-section into low and high bins based on the total invariant mass and p_T spectra. The new physics effects are further constrained by including extra kinematic information. However, some degeneracy persists, as shown in previous studies, especially in determining the Higgs trilinear coupling. Our analysis shows that the degeneracy is reduced by including the full NLO corrections.

Keywords: Higgs Pair Production, NLO, New Physics

I. INTRODUCTION

In 2012, a new scalar resonance^{1,2} with a mass of 125.09 ± 0.24 GeV³ was discovered at the Large Hadron Collider (LHC). After analyzing all the Run I data, the Standard Model (SM) Higgs boson provides best explanation for the measured properties of the new particle^{4–9}. Since then, high priority analyses at the Large Hadron Collider (LHC) always include the detailed study of the properties of this particle.

Theoretical uncertainties limit the reachable accuracies at the LHC. However, a wider range of Higgs couplings investigated at the LHC, and the increase of the variety of processes that involves the Higgs boson can partially compensate for this restriction. Currently, the most constrained condition is the gauge-Higgs coupling $C_v \equiv g = 0.94 + 0.11$, which is very close to the SM expectation. Furthermore, due to the fact that the observed Higgs candidate particle is produced at roughly the SM rate, the extensions of the Higgs sector beyond the Standard Model are extremely constrained. A simple model with a fourth generation of heavy quarks, for example, is excluded by the limits on Higgs production for any Higgs mass below around 600 GeV^{10,11} since such model predicts large deviations in the Higgs production rates from SM value^{12–16}. Unlike C_v , the Yukawa couplings of top-Higgs and bottom-Higgs are not constrained precisely by the data up to date. Moreover, they are within 30 – 40% of the SM expectations^{17,18}.

Testing the Higgs boson's self-interactions is particularly interesting. It is the only unmeasured experimentally property of the Higgs boson and provides the only window to probe the Higgs scalar potential, which is the origin of spontaneous symmetry breaking of the gauge symmetry and the origin of the particle masses in the Standard Model.

^{a)}Electronic mail: bhuang9@uic.edu

One of the most promising probes for LHC is the Higgs pair production. These processes provide direct measurements of the trilinear Higgs self-couplings at leading-order. Moreover, these processes complement indirect effects caused by the self-interactions of Higgs bosons in single-Higgs processes and radiative corrections to electroweak observables^{19,20} contaminated by possible interference effects with different models of New Physics.

Unfortunately, the Standard Model expectation of this production rate is only 0.034 pb at the Large Hadron Collider with CM energy equal to 14 TeV²¹. One of the reasons for such a low rate is that the SM contributions from the box diagram and the triangle diagram (shown in Fig. 1(a) and (b), respectively) interfere destructively near kinematic threshold²². However, the Standard Model cross-section rises dramatically to 1.54 pb at a future 100 TeV proton-proton collider since the luminosity increases in the parton distribution function of gluon at lower x , the Bjorken scale, this provides a chance to measure the Higgs self-couplings precisely^{23,24}.

Four major classes of processes are responsible for the production of Higgs pair at hadron colliders. First, we have $gg \rightarrow HH$, the gluon fusion process, with a loop of heavy quark, which has a strong coupling to the Higgs boson^{25–28}. The second class is $qq' \rightarrow qq'V^*V^* \rightarrow qq'HH$ ($V = Z, W$), the vector bosons fusion (VBF) processes, which generate two jets and two Higgs bosons in the final state^{25,29–32}. The third class is $q\bar{q}' \rightarrow V^* \rightarrow VHH$ ($V = Z, W$), the double Higgs-strahlung process, where a vector boson, W or Z , radiates the Higgs bosons³³. The last one has associated producing a pair of top quarks with two Higgs bosons, $pp \rightarrow t\bar{t}HH$ ³⁴.

Compared to single Higgs production, these processes have at least two orders of magnitude smaller production cross-sections as the phase space is small since the final state consists of two heavy particles. They have electroweak couplings of higher-order. Besides, other topologies which are irrelevant to the trilinear Higgs coupling, where the gauge boson or fermion lines radiate both Higgs bosons, which produce the same final state as the diagrams with $H^* \rightarrow HH$ splitting. Thus, these topologies pollute the correlation between the g_{H^3} coupling and the double Higgs production rate. It is extremely difficult to measuring the trilinear Higgs coupling, and very high energies along with very high collider luminosities are therefore required.

A. Next-to-Leading Order and Beyond Standard Model

It is almost impossible to measure the quartic Higgs coupling, g_{H^4} , in the near future as an extra v further suppresses it in the denominator compared to the trilinear Higgs self-coupling, and the smallness of the triple-Higgs production rate prohibit it from being probed directly^{35–39,40}. We can directly measure the trilinear Higgs coupling through Higgs-pair production, where Higgs pairs are dominantly produced in the gluon-fusion process mediated mainly by top-quark loops while the contribution of b -quark loops is negligible. Two types of diagrams, triangle, and box, contribute to the gluon-fusion process $gg \rightarrow HH$, where the triangle diagrams involve the trilinear Higgs coupling, and the interference between the one-loop box and triangle diagrams are destructive^{26,28}. The dominant contributions to the cross-section come from the box diagrams. The approximate relation, $\Delta\sigma/\sigma \sim -\Delta g_{H^3}/g_{H^3}$, gives a rough estimate of the correlation of the size of the trilinear Higgs self-coupling in the vicinity of the SM value of g_{H^3} and the cross-section. Therefore, small uncertainties of the relevant cross-section, which can be achieved by calculating higher-order corrections, are required to determine the trilinear Higgs coupling. The next-to-leading order (NLO) QCD corrections^{41–43} and next-to-next-to-leading order (NNLO) corrections, which adopt heavy top quark approximation^{44–46}, are fully known. The NLO corrections are significant, and therefore must be included. In comparison with NLO corrections, the NNLO contributions are much smaller but still considerable. The QCD next-to-next-to-next-to-leading order (N³LO) corrections to the effective couplings of Higgs and Higgs-pair to gluons are recently computed in heavy top quark approximation limit⁴⁷ and lead to a minor modification to the cross-section^{48–50}. The LO contributions and the higher-order

corrections contribute equally to the total production rate. Lately, the NLO results have been matched to parton showers^{51,52}, and the NLO mass effects with the additional top-mass effects in the double-real corrections have been merged with the full NNLO QCD results in the heavy-top limit⁵³. The full NLO QCD corrections to the Higgs-pair production rate with the anomalous trilinear Higgs self-coupling effects have been calculated in Ref. 21. In this work, we calculated full NLO results, including weak interaction contributions from $qg \rightarrow HHq$.

Although verifying that a scalar vev spontaneously breaks the electroweak symmetry is crucial, discovering new physics beyond the SM is always the final goal. Multiple new physics that could potentially affect this specific channel must be considered while analyzing the double Higgs production. One possible new physics from a new diagram involving the anomalous quartic coupling, $HH\bar{t}t$, as shown in Fig. 1(c) could give significant effect^{54–56}. The presence of this quartic coupling makes the total production rate insensitive to the Higgs self-coupling and makes measuring this coupling incredibly difficult⁵⁷.

B. Recent Searches in a Rare Particle Decay

The most significant double Higgs decay channel in the important low-mass region is the bottom quark pair plus photons pair channel, $HH \rightarrow \gamma\gamma b\bar{b}$. Recently, new analysis techniques for searching this rare process have been developed by physicists in ATLAS collaboration. To optimize the sensitivity to the self-coupling of Higgs bosons, they first split the pp collision events into low and high invariant mass groups. After that, they used a multivariate discriminant (Boosted Decision Tree) to separate the events that can be categorized as the $HH \rightarrow \gamma\gamma b\bar{b}$ process from those that can not. Finally, the Higgs-pair production rate is determined first, and then they observed how the production rate varies as a function of the Higgs self-coupling to its SM value ratio λ/λ_{SM} . By using the above procedures, the ATLAS team constrained the Higgs self-coupling and allowed it to vary between -1.5 and 6.7 times the SM value. Physicists, therefore, can set a currently best limit on the Higgs pair production rate of 4.1 times the SM value.

However, the work is far from being done. A huge amount of data is required to precisely measure the Higgs self-coupling and see if it were close to its SM value. The High-Luminosity upgrade of the LHC, scheduled to be operational in the late 2020s, is planned to operate at higher collision energy and deliver a dataset 20 times larger than used in this analysis. The Higgs pair production will be observed in this huge dataset if the Higgs pair production indeed behaves as predicted by the Standard Model, and a more quantitative statement will be made on the strength of the Higgs self-coupling.

C. Overview of This Thesis

This paper aims to learn how multiple new physics effects interplay in different kinematic distributions and the total cross-section at next-to-leading order. To research the topic more thoroughly, we also study the distributions of differential cross-sections, especially the invariant mass of the Higgs pair, m_{HH} , and the transverse momentum p_T . We study the LHC at center-of-mass energies of 14 TeV and a planning 100 TeV pp collider in the project of Future-Circular-Collider (FCC)^{58,59}.

This thesis is organized as follows. In Section II, we present the conventions and notations. We present the details of our calculation at LO and NLO in Section III. Then we study the influence of the new physics effects on the kinematic distributions in Section IV, and a numerical study on constraints using the kinematic information in a 100 TeV proton-proton collider. Finally, the conclusions are given in Section VII.

II. LEADING-ORDER CROSS-SECTION

SM contributions to calculations of Higgs pair production have been made a while back in Ref. 26 and 28. Also, the extra contribution from the anomalous $HHtt$ coupling has been studied in Ref. 54 and 55. At the leading-order, the production of the Higgs pair through

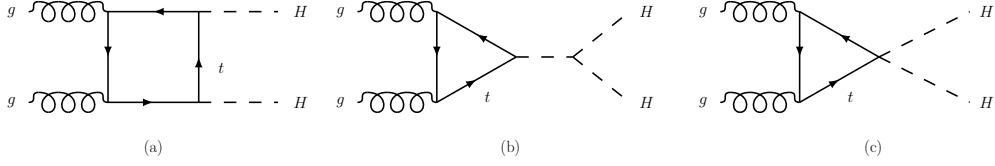


FIG. 1. *Feynman diagrams for loop-induced Higgs pair production through gluon fusion. Diagrams (a), b are SM diagrams, where (c) is BSM diagram with anomalous $HHtt$ coupling.*

gluon fusion is shown in Fig. 1, including each permutation of the external lines. The box diagram has no Higgs self-coupling, and the triangle diagram involves the Higgs trilinear coupling. We can write the matrix element of $g(p_1)g(p_2) \rightarrow H(p_3)H(p_4)$ at LO as

$$\mathcal{M}(g^a g^b \rightarrow HH) = -i \frac{\alpha_s(\mu_R) G_F m_{HH}^2}{2\sqrt{2}\pi} \mathcal{A}^{\mu\nu} \epsilon_{1\mu} \epsilon_{2\nu} \delta_{ab}$$

$$\text{with} \quad \mathcal{A}^{\mu\nu} = F_1 T_1^{\mu\nu} + F_2 T_2^{\mu\nu},$$

$$F_1 = \left(g_{H^3} \frac{1}{\hat{s} - m_H^2} g_{Htt} + g_{HHtt} \right) \frac{v^2}{m_t} F_{\Delta} + g_{Htt}^2 \frac{v^2}{m_t^2} F_{\square}, \quad (1)$$

$$F_2 = g_{Htt}^2 \frac{v^2}{m_t^2} G_{\square},$$

where m_{HH} is the invariant mass of the Higgs pair, a, b are the color indices of the initial gluons, $\alpha_s(\mu_R)$ is the strong coupling evaluated at the renormalization scale μ_R , and G_F is the Fermi constant.

The couplings g_{H^3} , g_{Htt} and g_{HHtt} denote the trilinear Higgs self-coupling, the top-Higgs coupling, and the anomalous nonlinear $HHtt$ coupling, respectively. The Lagrangian that involves these couplings reads

$$\frac{1}{3!} g_{H^3} H^3 + g_{Htt} H \bar{t} t + \frac{1}{2!} g_{HHtt} H^2 \bar{t} t. \quad (2)$$

Therefore in the SM we have

$$g_{H^3}^{(SM)} = \frac{3m_H^2}{v}, \quad g_{Htt}^{(SM)} = \frac{m_t}{v}, \quad g_{HHtt}^{(SM)} = 0, \quad (3)$$

where $v = 246$ GeV is the vacuum expectation value of the Higgs field.

The contributions of the two tensor structures, $T_1^{\mu\nu}$, correspond to the total angular-momentum states with $S_z = 0$ while $T_2^{\mu\nu}$ corresponds to $S_z = 2$,

$$T_1^{\mu\nu} = g^{\mu\nu} - \frac{p_1^\nu p_2^\mu}{(p_1 \cdot p_2)},$$

$$T_2^{\mu\nu} = g^{\mu\nu} + \frac{M_H^2 p_1^\nu p_2^\mu}{p_T^2 (p_1 \cdot p_2)} - 2 \frac{(p_2 \cdot p_3) p_1^\nu p_3^\mu}{p_T^2 (p_1 \cdot p_2)} - 2 \frac{(p_1 \cdot p_3) p_3^\nu p_2^\mu}{p_T^2 (p_1 \cdot p_2)} + 2 \frac{p_3^\nu p_3^\mu}{p_T^2}$$

$$\text{with} \quad p_T^2 = 2 \frac{(p_1 \cdot p_3)(p_2 \cdot p_3)}{(p_1 \cdot p_2)} - M_H^2, \quad (4)$$

where p_T is the transverse momentum of each Higgs boson in the final-state.

Here we follow the notations used in Ref. 28, the form factors for $gg \rightarrow HH$ are

$$\begin{aligned}
F_\Delta &= \frac{2}{S} [2 + (4 - S)m_t^2 C_{12}] \\
F_\square &= \frac{1}{S^2} \{ 4S + 8Sm_t^2 C_{12} - 2Sm_t^4 (S - 8 + 2R_{H/t}^2)(D_{123} + D_{213} + D_{132}) \\
&\quad + (2R_{H/t}^2 - 8)m_t^2 [\bar{T}(C_{13} + C_{24}) + \bar{U}(C_{23} + C_{14}) \\
&\quad - (TU - R_{H/t}^4)m_t^2 D_{132}] \} \\
G_\square &= \frac{1}{S(TU - R_{H/t}^2)} \{ (T^2 - 8T + R_{H/t}^2)m_t^2 (C_{12} + \bar{T}(C_{13} + C_{24}) - STM_t^2 D_{213}) \\
&\quad + m_t^2 (U^2 - 8U + R_{H/t}^2)(SC_{12} + \bar{U}(C_{23} + C_{14}) - SUM_t^2 D_{123}) \\
&\quad - m_t^2 (T^2 + U^2 - 2R_{H/t}^2)(T + U - 8)C_{cd} \\
&\quad - 2m_t^2 (TU - R_{H/t}^2)(D_{123} + D_{213} + D_{132}) \},
\end{aligned}$$

where

$$\hat{s} = (p_1 + p_2)^2, \quad \hat{t} = (p_3 - p_1)^2, \quad \hat{u} = (p_3 - p_2)^2$$

$$S = \hat{s}/m_t^2, \quad T = \hat{t}/m_t^2, \quad U = \hat{u}/m_t^2$$

$$R_{H/t} = m_H^2/m_t^2, \quad \bar{T} = T - R_{H/t}, \quad \bar{U} = U - R_{H/t}, \quad ,$$

and the scalar integrals:

$$\begin{aligned}
C_{ij} &= \int \frac{d^4 q}{i\pi^2} \frac{1}{(q^2 - m_Q^2) [(q + p_i)^2 - m_Q^2] [(q + p_i + p_j)^2 - m_Q^2]} \\
D_{ijk} &= \int \frac{d^4 q}{i\pi^2} \frac{1}{(q^2 - m_Q^2) [(q + p_i)^2 - m_Q^2] [(q + p_i + p_j)^2 - m_Q^2] [(q + p_i + p_j + p_k)^2 - m_Q^2]}
\end{aligned}$$

Notice that the loop function of the single Higgs production from the gluon fusion appears again in both Fig. 1(b) and Fig. 1(c). Only the loops involving SM top quark are considered in this work due to the smallness of Higgs couplings to other quarks.

For the three diagrams in Fig. 1, we can therefore express the partonic differential cross-section as

$$\begin{aligned}
\frac{d\hat{\sigma}(gg \rightarrow HH)}{d\hat{t}} &= \frac{G_F^2 \alpha_s^2}{512(2\pi)^3} \\
&\times \left[\left| \left(g_{H^3} \frac{1}{\hat{s} - m_H^2} g_{Htt} + g_{HHtt} \right) \frac{v^2}{m_t} F_\Delta + g_{Htt}^2 \frac{v^2}{m_t^2} F_\square \right|^2 + \left| g_{Htt}^2 \frac{v^2}{m_t^2} G_\square \right|^2 \right]. \quad (5)
\end{aligned}$$

In the SM Eq. (5) reduces to

$$\frac{G_F^2 \alpha_s^2}{512(2\pi)^3} \left[\left| \frac{3m_H^2}{\hat{s} - m_H^2} F_\Delta + F_\square \right|^2 + |G_\square|^2 \right]. \quad (6)$$

We can parameterize Eq. (5) with three dimensionless coefficients

$$\frac{d\hat{\sigma}(gg \rightarrow HH)}{d\hat{t}} = \frac{G_F^2 \alpha_s^2}{512(2\pi)^3} \left[\left| \left(c_{3H} \frac{3m_H^2}{\hat{s} - m_H^2} + c_{HHtt} \right) F_\Delta + c_{Htt} F_\square \right|^2 + |c_{Htt} G_\square|^2 \right]. \quad (7)$$

In SM, these coefficients reads

$$c_{3H}^{(SM)} = 1, \quad c_{Htt}^{(SM)} = 1, \quad c_{HHtt}^{(SM)} = 0. \quad (8)$$

The definition of these coefficients are⁶⁰

$$c_{3H} = g_H^3 g_{Htt} \frac{v^2}{3m_H^2 m_t}, \quad c_{HHtt} = g_{HHtt} \frac{v^2}{m_t}, \quad c_{Htt} = \left(g_{Htt} \frac{v}{m_t} \right)^2. \quad (9)$$

Only gauge-invariant operators of dimension-6 or higher lead to new physics effects of low-energy Higgs observables in the effective theory framework. We expect the importance of operators with mass dimensions greater than four to become less for lower energy scale. For dimension-6 operators, we have

$$\delta c_{3H, Htt, HHtt} \sim \mathcal{O} \left(\frac{v^2}{\Lambda_{np}^2} \right), \quad (10)$$

where $v = 246$ GeV, and Λ_{np} denotes the generic scale of new physics. A bottom-up approach is adopted in this work while c_{3H} , c_{Htt} , and c_{HHtt} are allowed to vary, without the constraints of the power counting in Eq. (10).

Eq. (7) is a quite general expression and includes new physics effects from various models. Provided that there are fermions with new color while coupled to the Higgs strongly. In that case, we can include the contributions from these new colors to $gg \rightarrow HH$ by applying the mass eigenvalues in the loop functions and calculating the Higgs couplings from the eigenbasis of masses. It is known that the $m_t \rightarrow \infty$ limit gives good approximations in F_Δ but works terribly in F_\square and G_\square ^{61,62}. It is known that the $m_t \rightarrow \infty$ limit gives good approximations in F_Δ but works terribly in F_\square and G_\square ^{61,62}. Roughly speaking, this is because the partonic CM energy is the Higgs pair invariant mass, \hat{s} , and is always above $4m_h^2$, the kinematic threshold, while the relation $\hat{s} \ll 4m_t^2$ is required in the low-energy Higgs theorems⁶³. Therefore, the complete mass dependence must be kept in the loop functions for scenarios with new colored particles, which have been studied thoroughly in Ref. 54 and 62.

III. CORRECTIONS UP TO NEXT-TO-LEADING-ORDER

Generically, the cross-section of double Higgs production up to next-to-leading-order can be expressed as²¹

$$\sigma_{NLO}(pp \rightarrow HH + X) = \sigma_{LO} + \Delta\sigma_{virt} + \Delta\sigma_{gg} + \Delta\sigma_{gq} + \Delta\sigma_{q\bar{q}}.$$

Here we define

$$\begin{aligned} \sigma_{LO} &= \int_{\tau_0}^1 d\tau \frac{d\mathcal{L}^{gg}}{d\tau} \hat{\sigma}_{LO}(Q^2 = \tau s), \\ \Delta\sigma_{virt} &= \frac{\alpha_s(\mu_R)}{\pi} \int_{\tau_0}^1 d\tau \frac{d\mathcal{L}^{gg}}{d\tau} \hat{\sigma}_{virt}(Q^2 = \tau s), \\ \Delta\sigma_{ij} &= \frac{\alpha_s(\mu_R)}{\pi} \int_{\tau_0}^1 d\tau \frac{d\mathcal{L}^{ij}}{d\tau} \int_{\tau_0/\tau}^1 \frac{dz}{z} \hat{\sigma}_{ij}(Q^2 = z\tau s) \quad (ij = gg, gq, q\bar{q}), \end{aligned} \quad (11)$$

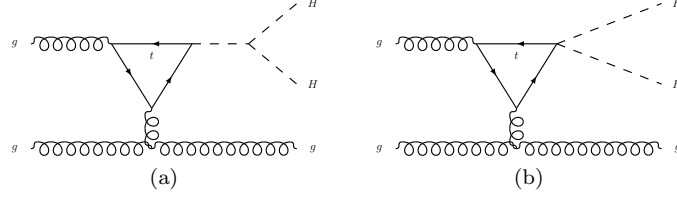


FIG. 2. Generic triangle diagrams for the partonic $gg \rightarrow HHg$ channel at NLO in QCD. Diagram (a) is SM diagrams, where (b) is BSM diagram with anomalous $HHtt$ coupling. Each gluon can be one of the two incoming gluons or the outgoing gluon.

where $\hat{\sigma}_{LO/virt/ij}(Q^2)$ denote the partonic cross-sections. The parton-parton luminosities are denoted by $d\mathcal{L}^{ij}/d\tau$ ($i, j = g, q, \bar{q}$), which is defined as

$$\begin{aligned} \frac{d\mathcal{L}^{gg}}{d\tau} &= \int_{\tau}^1 \frac{dx}{x} \left[g(x, \mu_F) g\left(\frac{\tau}{x}, \mu_F\right) \right], \\ \frac{d\mathcal{L}^{gq}}{d\tau} &= \sum_{q, \bar{q}} \int_{\tau}^1 \frac{dx}{x} \left[g(x, \mu_F) q\left(\frac{\tau}{x}, \mu_F\right) + q(x, \mu_F) g\left(\frac{\tau}{x}, \mu_F\right) \right], \\ \frac{d\mathcal{L}^{q\bar{q}}}{d\tau} &= \sum_q \int_{\tau}^1 \frac{dx}{x} \left[q(x, \mu_F) \bar{q}\left(\frac{\tau}{x}, \mu_F\right) + \bar{q}(x, \mu_F) q\left(\frac{\tau}{x}, \mu_F\right) \right], \end{aligned} \quad (12)$$

where $q(x, \mu_F)$ and $g(x, \mu_F)$ are the quark and gluon densities at the factorization scale μ_F .

A. $g g \rightarrow H H g$

Fig. 2 to Fig. 4 show the generic diagrams for the $gg \rightarrow HHg$ channel. For diagrams shown in Fig. 2, Fig. 3 (a), and Fig. 3 (b), the matrix elements can be easily obtained by replacing one on-shell gluon, ϵ_{ν} , with a gluon propagator and attaching the other end to a tri-gluon vertex in Eq. (2). The generic amplitude for these contributions can be written as

$$\begin{aligned} \mathcal{M}(g_1^{c_1} g_2^{c_2} \rightarrow HHg_3^{c_3}) &= -\frac{G_F \alpha_s(\mu_R) Q^2}{2\sqrt{2}\pi} \sum_{i,j,k} f^{c_i, c_j, c_k} \mathcal{A}^{\rho\alpha} \epsilon_{i\mu} \epsilon_{j\nu} \epsilon_{k\alpha} \frac{4\pi\alpha_s}{(p_i + p_j)^2} \\ &\quad \times [g_{\mu\nu}(p_i - p_j)^{\rho} + g_{\nu\rho}(2p_j + p_i)^{\mu} - g_{\rho\mu}(2p_i + p_j)^{\nu}], \end{aligned} \quad (13)$$

where gluons are labeled by $i, j, k \in 1, 2, 3$, c_i, p_i denotes the color index and the momentum of gluon labeled by i respectively and $\mathcal{A}^{\rho\alpha}$ is defined in Eq. (2).

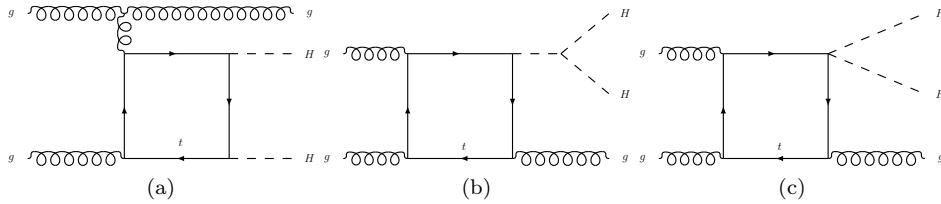


FIG. 3. Generic box diagrams for the partonic $gg \rightarrow HHg$ channel at NLO in QCD. Diagrams (a) and (b) are SM diagrams, where (c) is BSM diagram with anomalous $HHtt$ coupling. Each gluon can be one of the two incoming gluons or the outgoing gluon.

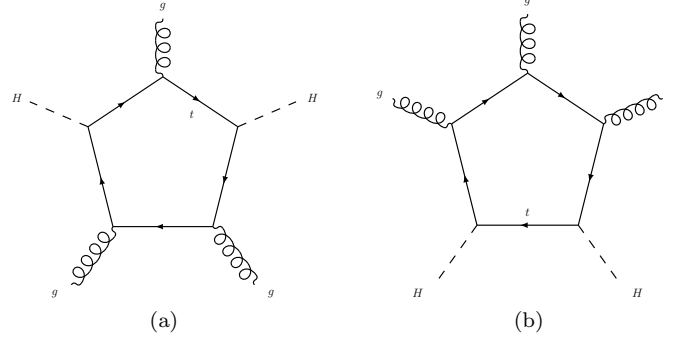


FIG. 4. Generic SM one-loop pentagon diagrams for the partonic $gg \rightarrow HHg$ channel at NLO in QCD. Each gluon can be one of the two incoming gluons or the outgoing gluon.

B. $qg \rightarrow HHq$ and $q\bar{q} \rightarrow HHg$

Although the contributions from $qg \rightarrow HHq$ and $q\bar{q} \rightarrow HHg$ are very different, as we will see in the next section, they share the same diagrams. Therefore, we only need to compute the matrix elements for $qg \rightarrow HHq$ which can be easily converted to corresponding matrix elements for $q\bar{q} \rightarrow HHg$. For contributions shown in Fig. 5, similar to the process $gg \rightarrow HHg$, the matrix elements can be easily obtained by replacing the only incoming gluon, ϵ_ν , with a gluon propagator and attaching the other end to two fermions in Eq. (2). The amplitude for contributions shown in Fig. 5 can be written as

$$\mathcal{M}(q(p_1)g(p_2) \rightarrow q(p_3)HH) = -\frac{G_F\alpha_s(\mu_R)Q^2}{2\sqrt{2}\pi}\mathcal{A}^{\mu\nu}\epsilon_\mu\bar{v}(p_3)\gamma_\nu u(p_1)\frac{\sqrt{4\pi\alpha_s}}{(p_3-p_1)^3}, \quad (14)$$

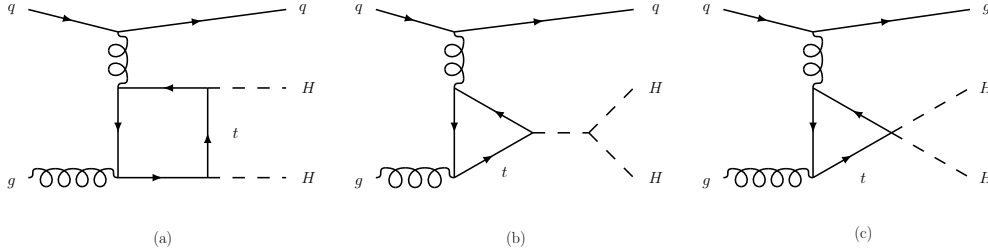


FIG. 5. Dominant box and triangle diagrams at the one-loop level for the $qg \rightarrow HHq$ channel.

Other than the common one-loop diagrams shown in Fig. 5. We also calculate the contributions from diagrams with only one strong coupling, which has not been studied before. We denote contributions from loop diagrams with more than one strong couplings as QCD_2 contribution and contributions from diagrams with only one strong coupling as QCD_1 contribution. As we will see in the next chapter, QCD_1 contribution is smaller compare to QCD_2 contribution due to the suppression from the weak coupling. For the production processes, $qg \rightarrow HHq$, tree-level diagrams are generally too small due to the smallness of the qqH coupling. Therefore, tree diagrams are usually dropped, and only the loop diagrams are considered. However, it turns out that we still have to consider tree diagram for $b(c)g \rightarrow b(c)HH$ shown in Fig. 6 since the contributions from loop diagrams are small and the bbH or ccH couplings are just large enough to make these tree diagrams contribute at similar order to loop-induced QCD_1 contributions.

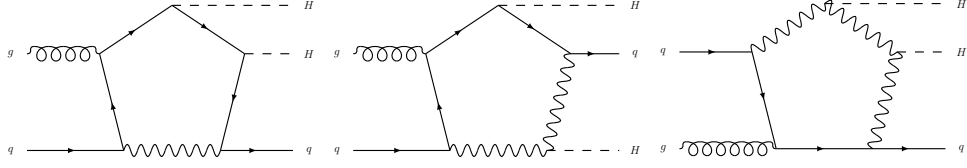
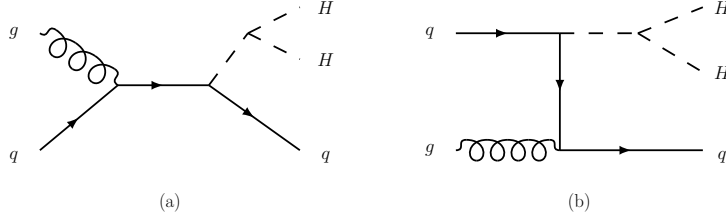


FIG. 7. Generic pentagon diagrams with different numbers of quarks and gauge bosons in the loop.

FIG. 6. Tree diagrams for $b(c)g \rightarrow b(c)HH$.

Again all diagrams to one loop level for $qg \rightarrow HHq$ can be categorized into the pentagon, box, and triangle diagrams. The pentagon, box, triangle diagrams are shown in Fig. 7 to Fig. 9, where solid lines and the wavy represent fermions and vector bosons (W , Z) or corresponding Goldstone boson($G^{+/-}$, G_0), respectively.

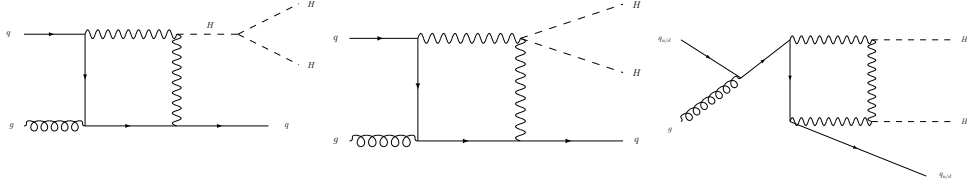


FIG. 8. Generic box diagrams with different numbers of quarks and gauge bosons in the loop.

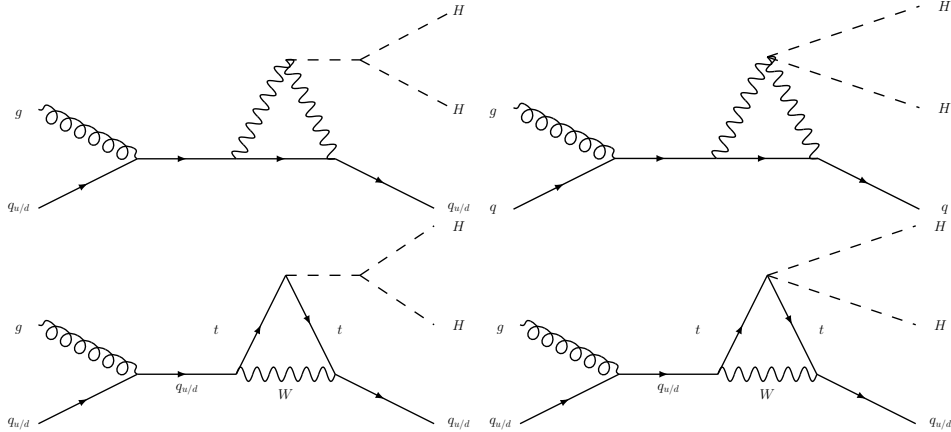


FIG. 9. Generic triangle diagrams with different numbers of quarks and gauge bosons in the loop.

For contributions from $gg \rightarrow HHg$ and $qg \rightarrow HHq$, we generate the full analytical one-loop matrix elements by using **FeynArts**⁶⁴ and **FormCalc**⁶⁵. The tensor reduction performed

by `FormCalc` is using the techniques developed in Ref. 66–69, while the numerical results of the scalar integrals⁷⁰ are evaluated with `LoopTools`⁶⁵. As cross-check, the analytic matrix elements for pentagon diagrams with two quark propagators in the loop, box diagrams with one quark propagator, and triangle diagrams are also calculated by hand. The results of matrix elements compute by hand, and matrix elements generated with `FeynArts` and `FormCalc` are in agreement with the numerical results generated by `MG5_aMC@NLO`⁷¹, which is the primary tool for the computations of cross-sections and the generation of hard events in this article.

IV. KINEMATIC DISTRIBUTIONS

We use the same workflow introduced in Section IV A, and adopt only `PDF4LHC15`⁷² to generate partonic events. For hadron level analysis, we feed the unweighted partonic events file into `Pythia` 8⁷³ to generate a large number of simulated collision events. To promptly analyze such a huge amount of simulated collision events, we adopt `Delphes`⁷⁴, which provides a fast multipurpose detector response simulation to reconstruct events into jets such as b jet and lepton jets, etc.

We analyzed the final results in detail for the total cross-section and the differential cross-section in the invariant mass of Higgs-pair.

For the double Higgs production with at most one extra jet, $pp \rightarrow HHj$, the SM expectation for this production cross-section is only 0.031 pb in the Large Hadron Collider with CM energy at 14 TeV. At the potential 100 TeV hadron collider, the expected SM cross-section increases significantly to 1.543 pb since the luminosity of gluon PDF at lower Bjorken scale, increases.

By convoluting the gluon and quark PDF's with the partonic cross-section in a hadron collider, we can obtain the differential cross-section in the lab frame

$$\frac{d^2\sigma(pp \rightarrow HH)}{dm_{HH} dp_T} = \int_{\tau}^1 \frac{dx}{x} g(x, \mu_F) g\left(\frac{\tau}{x}, \mu_F\right) \frac{2m_{HH}}{s} \frac{d\hat{\sigma}(gg \rightarrow HH)}{dp_T}, \quad (15)$$

where p_T is the transverse momentum of the Higgs boson, s is the CM energy of head-on hadrons, and $\tau = \hat{s}/s$, $m_{HH} = \sqrt{\hat{s}}$,

$$p_T^2 = \frac{\hat{u}\hat{t} - m_H^4}{\hat{s}}. \quad (16)$$

In this section, we firstly adopt `MG5_aMC@NLO`⁷¹ with a custom UFO model⁷⁵ including the anomalous Higgs-top coupling, $HHtt$, and corresponding R_2 and UV counterterms to generate matrix elements. We then adopt `PDF4LHC15`⁷² to generate partonic events. In this work, we draw all plots by using the framework above with the following parameters

$$m_t = 173\text{GeV}, \quad m_H = 125\text{GeV}. \quad (17)$$

The input value $\alpha_s(M_Z)$ is determined by the PDF set used, where $\alpha_s(M_Z) = 0.118$ for `PDF4LHC15`. We set the factorization and renormalization scales to $\mu_F = \mu_R = m_{HH}$.

A. Leading-order Contribution

In Fig. 10 we show the leading-order distributions of m_{HH} and p_T for the Standard Model $gg \rightarrow HH$ process in a proton-proton collider at CM energies of 14 and 100 TeV. We can see that the general shapes are insensitive to the CM energy of the pp collider for these kinematic distributions. The kinematic distributions peak at $m_{HH} \sim 420$ GeV for the invariant mass of the Higgs pair, and $p_T \sim 150$ GeV for the transverse momentum of the single Higgs boson.

The invariant mass of most events is remote above $2m_H$, the kinematic threshold of two outgoing Higgs bosons. Therefore, the low-energy Higgs theorem is invalid for $gg \rightarrow HH$, as mentioned at the end of Section II. The contribution from c_{3H} rises significantly as $m_{HH} \sim 2m_H$ since the coefficient of the loop function F_Δ is

$$c_{3H} \frac{3m_H^2}{\hat{s} - m_H^2} + c_{HHtt}. \quad (18)$$

As a result, c_{HHtt} could become dominant over c_{3H} at large m_{HH} . Unfortunately, the total cross-section contribution from c_{3H} will be suppressed since most of the events have $m_{HH} \gg 2m_H$, which was concluded in Ref. 57. Therefore, it will be very difficult to measure a truly model-independent Higgs trilinear coupling solely from the total cross-section of double Higgs production. Fig. 11 and Table I show the individual contribution from Triangle, Box and HHtt, defined in Eq. (20), and compare them with the SM expectation.

$$\begin{aligned} \text{Triangle : } c_{3H} &= 1, c_{Htt} = 0, c_{HHtt} = 0 \\ \text{Box : } c_{3H} &= 0, c_{Htt} = 1, c_{HHtt} = 0 \\ \text{HHtt : } c_{3H} &= 0, c_{Htt} = 0, c_{HHtt} = 1 \end{aligned} \quad (19)$$

The total cross-section contribution from the SM diagrams is relatively small when $c_{3H} \sim c_{Htt}$ due to the nature of destructive interference between the triangle and box diagrams, which can be inferred from Fig. 11. Consequently, the measurement of c_{3H} would be significantly impacted by turning on a small c_{HHtt} . Although there is a 30% difference in the total cross-section between two PDF sets, the general shapes of the kinematic distributions are not sensitive to the PDF set we use, and we will only show the results with PDF4LHC15 from now on.

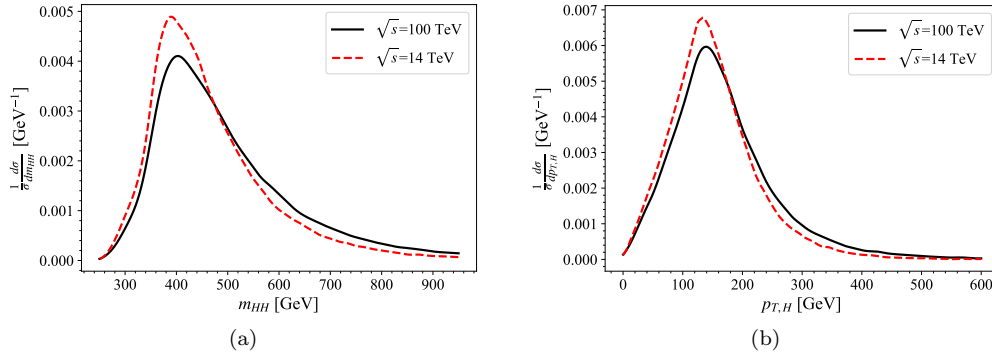


FIG. 10. The SM expectation of LO m_{HH} and $p_{T,H}$ distributions at $\sqrt{s} = 14$ and 100 TeV.

σ [pb]	Total	Triangle	Box	HHtt
14 TeV	0.0167	0.004692	0.0349	0.042
100 TeV	0.6923	0.146	1.32	1.98

TABLE I. Individual contribution of cross-section from Triangle, Box and HHtt in 14 and 100 TeV hadron colliders.

For p_T spectrum of individual contribution, G_\square has a strong p_T dependence, and p_T dependence in F_\square is not as strong as G_\square while F_Δ has no p_T dependence. This is because the projection of the angular momentum of head-on gluons with the same helicity on the beam axis is zero, $J_z = 0$, which corresponds to F_Δ and F_\square . On the other hand, G_\square has $J_z = 2$ on the beam axis resulted from opposite helicity gluons^{26,28}. Nevertheless, only the S -wave orbital angular momentum is contained by F_Δ since only the scalar Higgs couplings

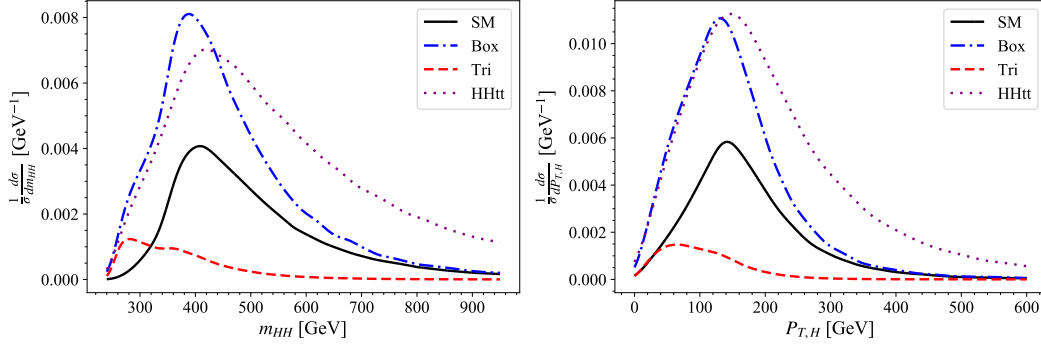


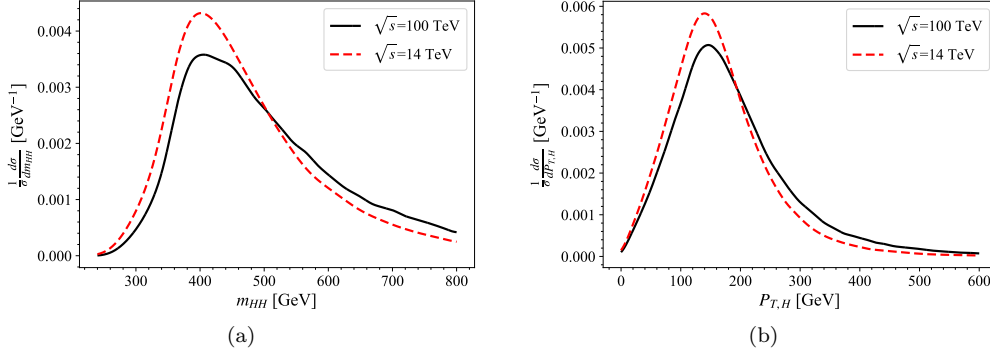
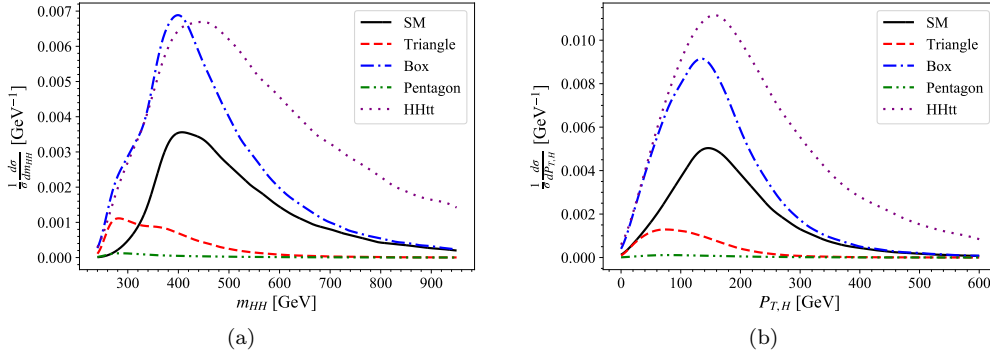
FIG. 11. Individual contribution from Triangle, Box, HHtt to the LO m_{HH} and $p_{T,H}$ distributions in a hadron collider at $\sqrt{s} = 100$ TeV. The results are obtained by adopting PDF4LHC15.

are included in Fig. 1(a) and Fig. 1(c). In other words, F_{Δ} is p_T independent. Therefore, the phase space is the only source of all the p_T dependence in the c_{3H} and c_{HHtt} . However, the higher-order terms of \hat{s}/m_t^2 expansion for the $J_z = 0$ component of the D -wave angular dependence leave some p_T dependence for F_{\square} ⁶². G_{\square} has a strong p_T dependence due to the D -wave nature. Furthermore, the difference of the angular momentum projection between F_{Δ}/F_{\square} and G_{\square} also explains the lack of interference between the two contributions in Eq. (5). in Fig. 11 we also show the p_T spectrum of individual contribution from Triangle, Box and HHtt. The contribution from Triangle are suppressed in general, as in the m_{HH} distribution since the Higgs propagator in Fig. 1(b) is off-shell.

B. $g g \rightarrow H H g$ Contribution

Numerical calculations of $g g \rightarrow H H g$ are performed in 14 and 100 TeV hadron colliders. The standard model (SM) expectation of the cross-section at a 14 TeV pp collider for this channel is 0.014 pb. At 100 TeV, the SM rate rises significantly to 0.85 pb. The contribution of the double Higgs production from $g g \rightarrow H H g$ is comparable to LO $g g \rightarrow H H$, 0.0167 pb and 0.692 pb at 14 and 100 TeV, respectively, and consist half of the total production rate.

In Fig. 12, we present the SM m_{HH} and p_T distributions for $g g \rightarrow H H g$ in 14 and 100 TeV hadron colliders. Since the dominant contributions come from one loop triangle and box diagrams shown in Fig. 2 and Fig. 3 respectively, which has the same loop function as $g g \rightarrow H H$ channel. We therefore expect the general shapes of kinematic distributions shown in Fig. 14 are insensitive to the center-of-mass energy of the hadron collider and share some similarity to Fig. 10. Indeed, comparing to LO counterpart, the general shapes are very similar except they are wider.

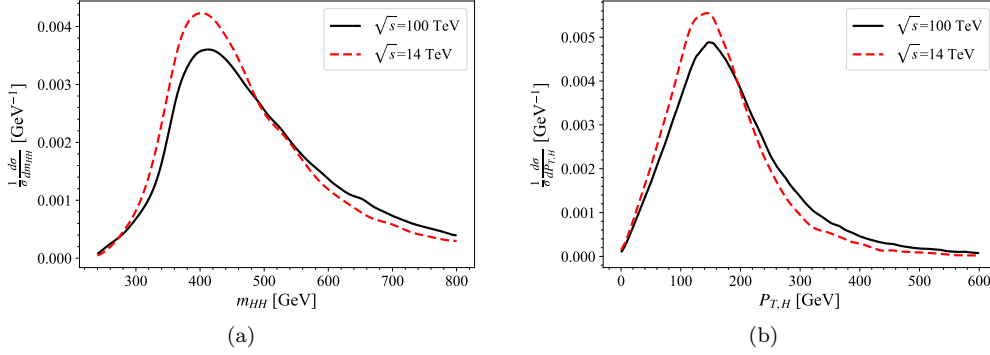
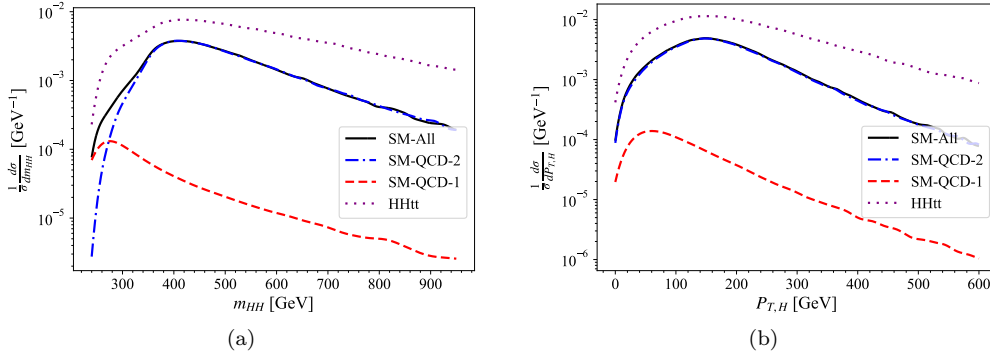
FIG. 12. Kinematic distributions for $gg \rightarrow HHg$ in the SM at $\sqrt{s} = 14$ and 100 TeV.FIG. 13. Individual contribution from Triangle, Box, Pentagon and HHtt to the kinematic distributions for $gg \rightarrow HHg$ in the SM at $\sqrt{s} = 100$ TeV.

The invariant mass distribution peaks at slightly lower $m_{HH} \sim 380$ GeV, while the maximum of p_T distribution is still at $p_T \sim 150$ GeV. Unlike the $gg \rightarrow HH$ counterpart, we can easily see the peaks in Fig. 10 move to the right slightly and get wider as the CM energy of the head-on hadrons increases. There are even more events that have $m_{HH} \gg 2m_H$. Hence the contribution to the total cross-section from c_{3H} will be further suppressed as we already discussed in Section IV A.

In Fig. 13 we show the individual contribution of $gg \rightarrow HHg$ channel from Triangle, Box, Pentagon, and HHtt diagrams, shown in Fig. 2 to Fig. 4, in the m_{HH} and P_T distribution while comparing them with the SM expectation. Triangle, box, pentagon contributions come from SM diagrams, while HHtt is the contribution from diagrams with anomalous $HHtt$ coupling. As we can see, $gg \rightarrow HHg$ have similar kinematic distributions and similar reactions to the parameters, c_{3H} , c_{Htt} , and c_{HHtt} , due to the same loop function in Eq. (5). The c_{3H} contribution to the total cross-section is still suppressed when $c_{3H} \sim c_{HHtt}$, and c_{HHtt} would have a significant impact on the cross-section of $gg \rightarrow HHg$ process as we saw in the LO case.

C. $qg \rightarrow HHq$ Contribution

For the $qg \rightarrow HHq$ process, we can categorize the contributions by the number of couplings to gluons. The contributions from diagrams with more than one strong couplings and contributions from diagrams with only one strong coupling are denoted as QCD_2 and QCD_1 , respectively.

FIG. 14. Kinematic distributions for $gg \rightarrow HHq$ in the SM at $\sqrt{s} = 14$ and 100 TeV.FIG. 15. Individual contribution from QCD_1 , QCD_2 , $HHtt$ to the kinematic distributions for $gg \rightarrow HHq$ in the SM at $\sqrt{s} = 100$ TeV.

In Fig. 14, we show the kinematic distributions, including m_{HH} and p_T , for SM $gg \rightarrow HHq$ in the hadron collider at CM energies 14 and 100 TeV. Since the dominant contributions come from one loop triangle and box diagrams shown in Fig. 5, which has the same loop function as $gg \rightarrow HH$, we expect Fig. 14 to share some similarity to Fig. 10. Comparing to $gg \rightarrow HH$ counterpart, the general shapes are very similar except they are wider. The maximum for invariant mass and p_T distributions are still the same, $m_{HH} \sim 420$ GeV and $p_T \sim 150$ GeV respectively. For most events, the invariant mass is far above the threshold, $2m_H$ as we already discussed in Section IV A. Unlike $gg \rightarrow HH$ counterpart, we can easily see the peaks in Fig. 10 move to the right slightly and get wider as the CM energy of the hadron collider increases. This means even more events have $m_{HH} \gg 2m_H$.

Fig. 15 shows the individual contribution of $gg \rightarrow HHq$ from QCD_2 , QCD_1 , and $HHtt$ in the m_{HH} and P_T distribution while comparing these contributions with the SM expectation. QCD_2 is the contribution from diagrams with more than one gluon coupling as shown in Fig. 5. QCD_1 contribution includes all the rest of SM diagrams for $gg \rightarrow HHq$, including tree, triangle, box, and pentagon diagrams, while $HHtt$ contribution comes from diagrams with an $HHtt$ coupling. As we can see, QCD_2 is the dominant contribution of $gg \rightarrow HHq$ since weak couplings suppress QCD_1 contribution. Again we can expect $gg \rightarrow HH$, $gg \rightarrow HHq$ have similar kinematic distributions and similar reactions to the parameters, c_{3H} , c_{HHtt} , and c_{HHtt} . We find the CM energy insensitivity of the general shapes of these distributions. Therefore, in what follows, we only present the result for $\sqrt{s} = 100$ TeV. As we saw in the $gg \rightarrow HH$ channel, the contribution self-coupling to the total cross-section from diagrams that involve the trilinear Higgs is still suppressed when $c_{3H} \sim c_{HHtt}$, and c_{HHtt} would have significant effects on the cross-section of the $gg \rightarrow HHq$ process.

For QCD_1 contribution, more events have lower invariant mass, m_{HH} , and transverse momentum, p_T . The peak of invariant mass distribution is at $m_{HH} \sim 280$ GeV, while the maximum of p_T distribution is at $p_T \sim 60$ GeV. Hence, the QCD_1 contribution at small invariant mass, $m_{HH} \sim 2m_H$, is more important than the QCD_2 contribution, which is dominant at large m_{HH} .

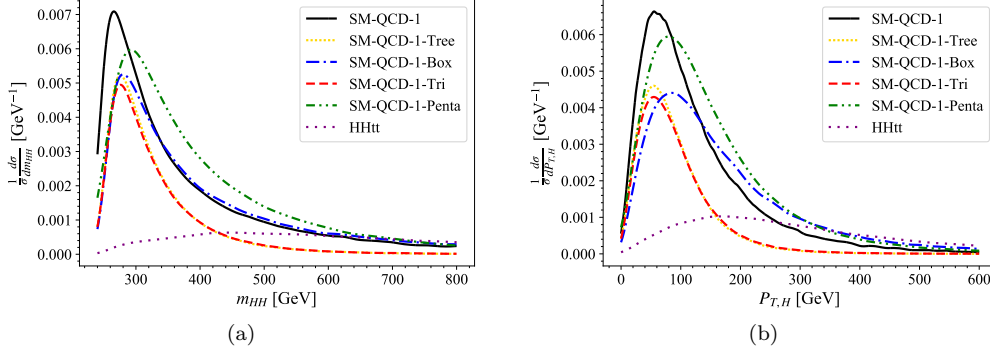


FIG. 16. Individual QCD_1 contribution from tree, triangle, box, pentagon diagrams to the kinematic distributions for $qg \rightarrow HHq$ in the SM at $\sqrt{s} = 100$ TeV.

In Fig. 16, for completeness, we further divide the QCD_1 contribution into the individual contribution from the tree, triangle, box, pentagon, and $HHtt$ contributions from corresponding diagrams and compare them with the total QCD_1 contribution. We can categorize individual contributions shown in Fig. 16 into two groups. Group one consists of tree and box diagrams, while group two consists of the triangle and pentagon diagrams. As a result, the interference between the contribution from group one and group two is destructive, which can also be inferred from Fig. 16. The $HHtt$ contribution when $c_{HHtt} = 1$ comes from diagrams with only one gluon coupling, as shown in Fig. 8 and Fig. 9 is very small compared to the QCD_1 contribution, which is already small. However, the $HHtt$ contribution shown in Fig. 15 is dominant over SM value. Therefore, most of $HHtt$ contribution to $qg \rightarrow HHq$ channel comes from diagrams shown in Fig. 5.

D. NLO

In Fig. 17, we show the individual SM contributions from all processes up to NLO, including $gg \rightarrow HH$, $gg \rightarrow HHg$, $qg \rightarrow HHq$ and $qg \rightarrow HHg$, while comparing them with the total NLO SM contributions in the m_{HH} and p_T distribution.

We can see that $gg \rightarrow HH$ and $gg \rightarrow HHg$ contributions are equivalently dominant while $qg \rightarrow HHq$ only contributes about 10% of the total cross-section. Similar kinematic distributions to $gg \rightarrow HH$ contribution are found in $gg \rightarrow HHg$ and $qg \rightarrow HHq$ contributions. We can therefore expect the full NLO contribution have similar kinematic distributions and similar reactions to the parameters. As expected, The peaks of invariant mass and p_T are still at $m_{HH} \sim 420$ GeV and $p_T \sim 150$ GeV, respectively.

The parameters we previously used, c_{3H} , c_{Htt} and c_{HHtt} , have to be generalized since the contributions from diagrams such as Fig. 8 do not have HHH , Htt , or $HHtt$ couplings. By following the same idea, we can create a new parameter set based on all Higgs couplings c_{3H} , c_{Htt} , c_{HHtt} , c_{HWW} , c_{HZZ} , $c_{HZZ,Htt}$, and $c_{Hbb(cc)}$ such that

$$\begin{aligned} \mathcal{M} = & c_{3H}\mathcal{M}_{3H} + c_{Htt}\mathcal{M}_{Htt} + c_{HHtt}\mathcal{M}_{HHtt} + c_{HWW}\mathcal{M}_{HWW} \\ & + c_{HZZ}\mathcal{M}_{HZZ} + c_{HZZ,Htt}\mathcal{M}_{HZZ,Htt} + c_{Hbb(cc)}\mathcal{M}_{Hbb(cc)}, \end{aligned} \quad (20)$$

where

$$\begin{aligned}
c_{3H} &= g_H^3 g_{Htt} \frac{v^2}{3m_H^2 m_t}, & c_{HHtt} &= g_{HHtt} \frac{v^2}{m_t}, & c_{Htt} &= \left(g_{Htt} \frac{v}{m_t} \right)^2 \\
c_{Hbb(cc)} &= \left(g_{Hbb(cc)} \frac{v}{m_b} \right)^2, & c_{HWW} &= \left(g_{HWW} \frac{v}{2m_W^2} \right)^2, & c_{HZZ} &= \left(g_{HZZ} \frac{v}{2m_Z^2} \right)^2 \\
c_{HWW,Htt} &= \left(g_{HWW} g_{Htt} \frac{v^2}{2m_W^2 m_t} \right)^2.
\end{aligned}$$

\mathcal{M}_x is amplitude of diagrams with coupling x while $\mathcal{M}_{HWW,Htt}/\mathcal{M}_{HZZ,Htt}$ is amplitude of diagram with HWW/HZZ and Htt couplings. If we adopt this new set of parameters into $gg \rightarrow HH$ channel, we can see that

$$c_{3H} = c_{3H}, \quad c_{Htt} = c_{Htt} \text{ and } c_{HHtt} = c_{HHtt}. \quad (21)$$

Fig. 18 shows the individual contribution from c_{3H} , c_{Htt} , c_{HHtt} , and the distribution of SM expectation in the m_{HH} and $p_{T,H}$ distribution. The Higgs low-energy theorem breaks down since most events have an invariant mass much higher than the kinematic threshold at $2m_H$ as discussed at the end of Section II. We note that c_{HHtt} is even more dominant over c_{3H} at large m_{HH} in Fig. 17 compare to $gg \rightarrow HH$ counterpart shown in Fig. 11. Turning on a small c_{HHtt} would significantly impact the measurement of c_{3H} when $c_{3H} \sim c_{Htt}$ since the contribution from the Higgs trilinear coupling to the total cross-section is relatively small, and the destructive interference between the box and triangle diagrams. These facts make a truly model-independent Higgs trilinear coupling measurement from the total rate of the Higgs pair production challenging since most of the events have $m_{HH} \gg 2m_H$, the contribution of the total cross-section from c_{3H} will be suppressed.

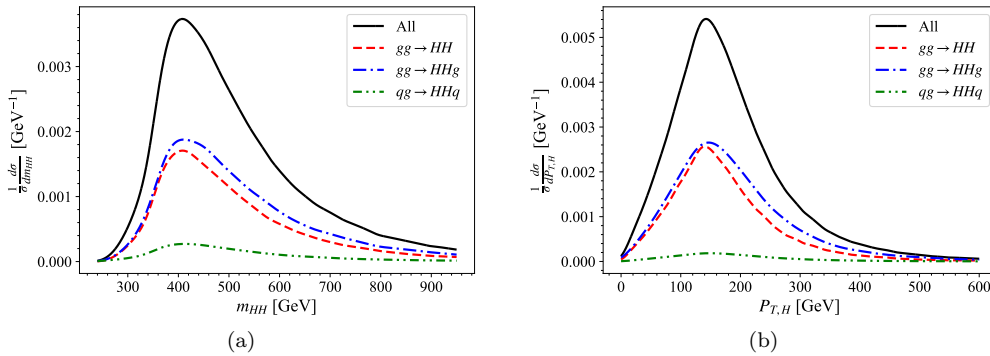


FIG. 17. Individual contribution from $gg \rightarrow HH$, $gg \rightarrow HHg$, $qg \rightarrow HHq$ to the kinematic distributions for double Higgs production in the SM at $\sqrt{s} = 100$ TeV.

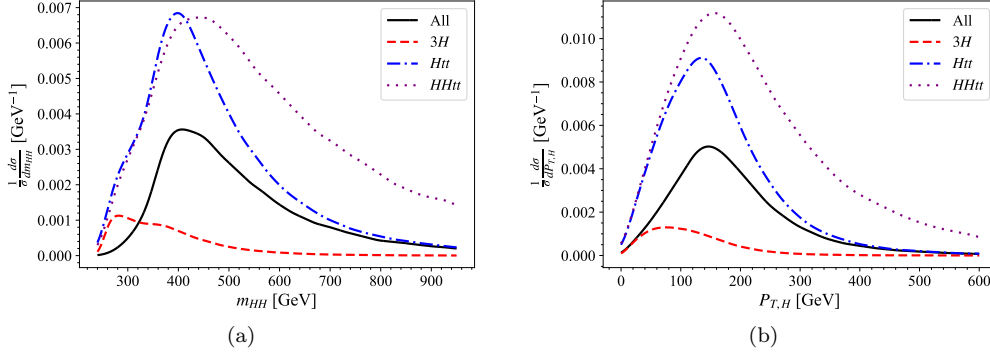


FIG. 18. Individual contribution from c_{3H} , c_{Htt} and c_{HHtt} to the kinematic distributions for double Higgs production at $\sqrt{s} = 100$ TeV.

V. THE $b\bar{b}\gamma\gamma$ DECAY CHANNEL

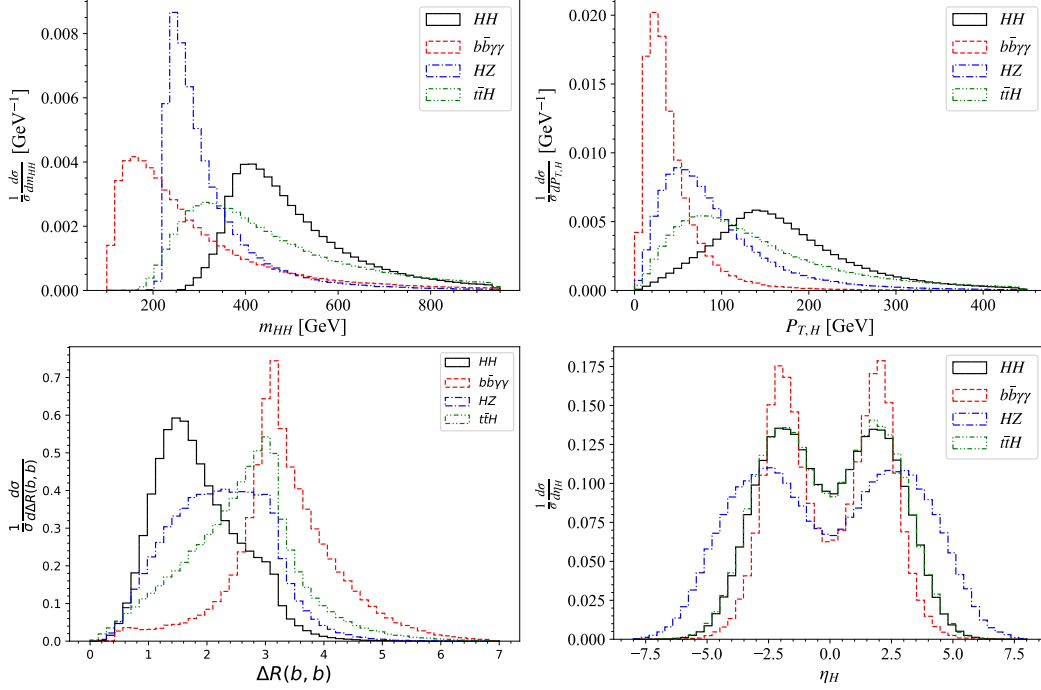
In this section, we investigate $HH \rightarrow b\bar{b}\gamma\gamma$ channel, which is the process that has the highest signal significance and in SM has the most sensitivity to the trilinear Higgs self-coupling as pointed out in the literature. Earlier studies can be found in Ref. 23, 76–79. Recent searches⁸⁰ for pairs of Higgs bosons in $HH \rightarrow \gamma\gamma b\bar{b}$ process have narrowed the upper bound of the Higgs pair production rate down to 4.1 times the SM expectation, created a portal of better understanding into the fundamental Higgs mechanism. We perform the partonic event generation for the signal and backgrounds by using **MadGraph5_aMC@NLO** with the parton density functions **PDF4LHC15**⁷². Parameters are kept the same as what we use in Eq. 17 with $\mu_R = \mu_F = m_{HH}$. The effects of full NLO corrections for the signal, $H(b\bar{b})H(\gamma\gamma)$, are included. We generate the background events at LO with the finite-top-mass effects and rescale them by a K -factor afterward (See Table II).

We include the following major backgrounds in the analysis: the resonant processes, $t\bar{t}\gamma\gamma$ and $t\bar{t}H(\gamma\gamma)$ with $t \rightarrow bW$ subdecay, as well as $b\bar{b}H(\gamma\gamma)$ and $Z(b\bar{b})H$, and the non-resonant processes $jj\gamma\gamma$ (with one and two fake b -jets), $b\bar{b}\gamma\gamma$, $b\bar{b}j\gamma$ (with one fake photon), $bj\gamma\gamma$. The $b\bar{b}jj$ background is not included since it is negligible compared to other faked backgrounds after selection cuts. The MLM matching is applied to all background processes with at most one extra parton to avoid double-counting.

We generate events with exclusive cuts for signal and background processes. In what follows, the acceptance cuts are applied to each final state for each plot. Here is the detailed event selection: We require exactly two b quarks and two photons in the final state with the following cuts $p_{T,b} > 30$ GeV, $|\eta_b| < 2.5$ and $\Delta R(b,b) > 0.4$, where the distance is defined as $\Delta R = \sqrt{(\Delta\eta)^2 + (\Delta\phi)^2}$. For leptons, the allowed soft transverse momentum and the allowed pseudorapidity are set to $p_{T,\ell} > 20$ GeV and $|\eta_\ell| < 2.5$, respectively, to diminish the $t\bar{t}H$ background. Moreover, the select events are selected to satisfy $|\eta_{jet}| < 2.5$ and $p_{T,jet} > 20$ GeV for QCD jets to diminish the $t\bar{t}H$ background further. The two photons has to fulfill $\Delta R(\gamma,\gamma) > 0.4$, $|\eta_\gamma| < 2.5$, and $p_{T,\gamma} > 30$ GeV. To reconstruct the Higgs bosons, the allowed invariant masses are within 25 GeV, $112.5 \text{ GeV} < M_{b\bar{b}} < 137.5 \text{ GeV}$ for the b quark pair, and a smaller range of 10 GeV, $120 \text{ GeV} < M_{\gamma\gamma} < 130 \text{ GeV}$ for the photon pair. In addition, we induce $\Delta R(\gamma,b) > 0.4$ to isolate the b quarks with the photons.

Besides the acceptance cuts shown above, more advanced cuts have been applied based on the distributions shown in Fig. 19 for the parton-level analysis. First, we select the events with a reconstructed invariant mass of the Higgs pair that satisfy $m_{HH} > 300$ GeV. Moreover, we select events that satisfy $P_{T,H} > 100$ GeV. We also require $\Delta R(b,b) < 2.5$ to divide the two b jet and require the reconstructed Higgs boson to have the pseudorapidity $|\eta_H| < 2$.

\sqrt{s} [TeV]	HH	$b\bar{b}\gamma\gamma$	$t\bar{t}H$	ZH	$b\bar{b}H$	$\gamma\gamma jj$	$b\bar{b}j\gamma$
100	1	1.0	1.3	1.2	0.87	1.43	1.08

TABLE II. K -factors for ZH , $b\bar{b}\gamma\gamma$ and $t\bar{t}H$ production at $\sqrt{s} = 100$ TeV⁸².FIG. 19. Normalized signal and backgrounds distributions of $P_{T,H}$, m_{HH} , R_{bb} and η_H in the $b\bar{b}\gamma\gamma$ channel at a $\sqrt{s} = 100$ TeV pp collider.

For the $b\bar{b}\gamma\gamma$ final state, a realistic estimation of the diphoton fake rate is the most important factor of an accurate assessment for measuring the signal since the production of multijet, which is the dominant background in this case, give rise to this fake rate.

To gain more reliable results and verify if any promising feature can be found in real experiments, we include showering and hadronization effects by using the **Pythia 8**⁷³ package⁷³ for the signal and background samples. Detector simulation effects based on the current performance of ATLAS and CMS are included by using the **Delphes**⁷⁴ package. We follow the parameter settings and the cut selections in Ref. 56. We chose the operation points of b -tagging to have 18.8%, 75%, and 1% for charm, bottom, and light quark jets in the central region, $|\eta| < 2.5$ and $P_{T,j} > 50$ GeV, respectively. The photon identification efficiency is about 80% for photons with $P_{T,\gamma} > 50$ GeV and $|\eta| < 2.5$. For the background with fake photons from misidentified jets, we assign a mistag rate of $f_j = 0.0093 \exp(-P_T/27)$ as a function of P_T in GeV of the jet with the fake photon energy equal to the jet energy scaled by 0.75 ± 0.12 ⁸¹. At $M_h = 125$ GeV, the mass resolution is 17 GeV for $h \rightarrow b\bar{b}$ and 2 GeV for $h \rightarrow \gamma\gamma$. In order to be consistent with the signal, the isolated photon pair and two tagged b -jets in the final states are selected to satisfy $P_T > 25$ GeV and $|\eta| < 2.5$.

The cuts for mass-window are further applied to the invariant-masses of the two photons and two b -jets. For the photon pair, we impose $122 \text{ GeV} < M_{\gamma\gamma} < 128 \text{ GeV}$ on the invariant-mass window. The invariant-mass window of the two b -jets is $120 \text{ GeV} < m_{b\bar{b}} < 130 \text{ GeV}$.

After applying the cuts shown in Table III, the final significance we obtained is $S/\sqrt{B} = 16.1$ for the integrated luminosity, $\int \mathcal{L} = 3 \text{ ab}^{-1}$, which is close to previous studies^{23,56}.

Observables	Acceptance cuts
Total number n of jets (j, γ, l)	$n < 7$ in each event
Pseudorapidity	$\eta_{b,\gamma} < 2.5$
Invariant mass	$120 < m_{b\bar{b}} < 130$ GeV, $122 < m_{\gamma\gamma} < 128$ GeV, $m_{b\bar{b}\gamma\gamma} > 300$ GeV
Transverse momentum	$p_{T\gamma,b} > 35$ GeV, $p_{T\gamma\gamma,b\bar{b}} > 100$ GeV
ΔR	$0.4 < \Delta R(b, b) < 2.0$, $0.4 < \Delta R(\gamma, \gamma) < 2.5$

TABLE III. List of observables and acceptance cuts used for the analysis.

This strongly suggests that the $b\bar{b}\gamma\gamma$ channel is observable in the future upgrade of the LHC (HE-LHC) or Future-Circular-Collider (FCC).

VI. SENSITIVITY TO EFFECTIVE SELF-COUPPLINGS OF HIGGS BOSONS

In this section, the characteristic distributions of the double Higgs production are studied for several observables with different values of effective Higgs couplings.

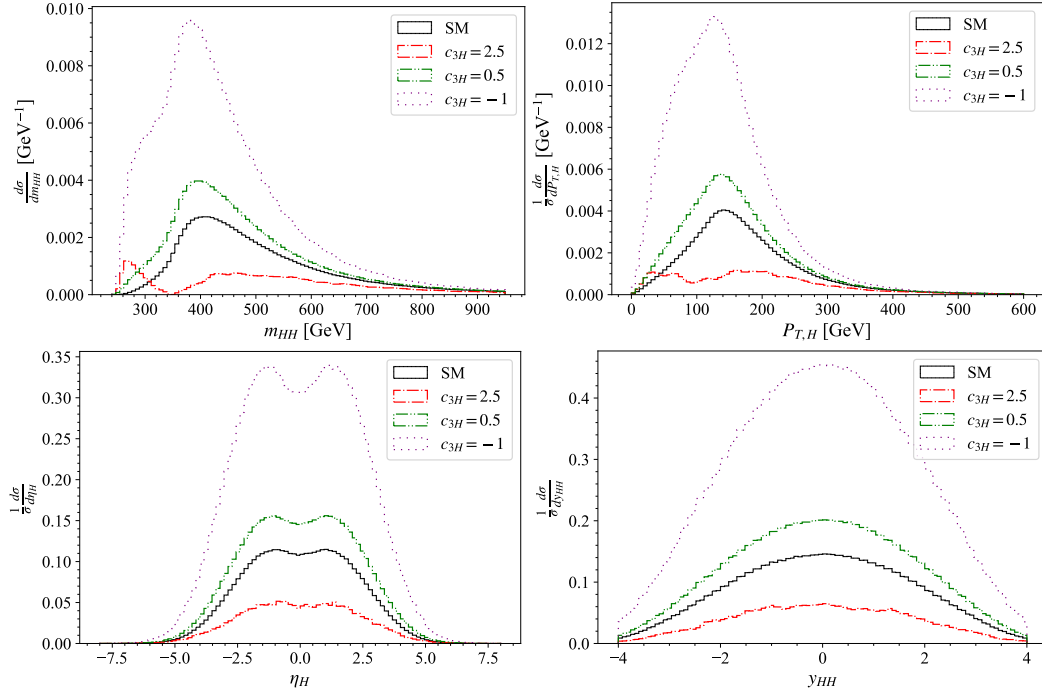
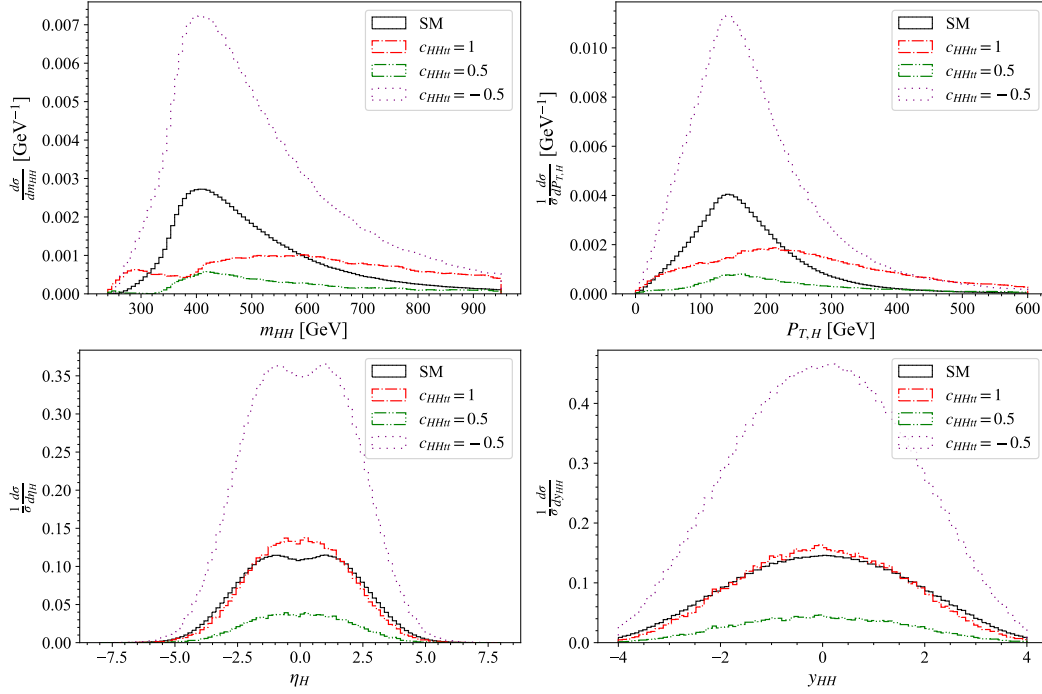
Fig. 20, shows the distributions of the invariant mass m_{HH} , the transverse momentum $P_{T,H}$, the pseudorapidity η_H , and the rapidity y_{HH} of the Higgs pair with the area under the SM curve normalized to unity. Each observable distribution is shown for $c_{3H} = 0.5, 1, 2.5$, and -1 .

As in the $P_{T,H}$ distribution plot of Fig. 20 with the distribution max at $P_{T,H} \sim 150$ GeV. The Higgs bosons from the production of inclusive Higgs pair are usually boosted. The pseudorapidity of the Higgs pair shown in the lower left of Fig. 20 is low and has a typical symmetric distribution with the maximum close to zero due to the high transverse momentum spectrum. For $c_{3H} = 2.5$, the interferences between the box and the triangle diagrams are destructive. This explains the dip in the $P_{T,H}$ distribution. Comparing to a lower peak value of $M_{ZH} \gtrsim 250$ GeV for the background shown in Fig. 19, the peak value is $m_{HH} \gtrsim 420$ GeV for the signal. Again, this destructive interference also causes a significant depletion in the signal when $c_{3H} = 2.5$. For smaller $c_{3H} = 0.5$, the destructive interference is diminished, and the signal is stronger than the SM expectation value for each distribution. For $c_{3H} = -1$, the differential cross-sections for all observables are enhanced significantly since the box diagram interferes constructively with the triangle diagram when c_{3H} becomes negative. For y_{HH} and η_H distribution, the overall shape is the same for different trilinear Higgs coupling values. We can infer that the y_{HH} distribution is significantly wider for the ZH background than for the signal shown in Fig. 19.

A similar distribution analysis is shown in Fig. 21 for $c_{HHtt} = -0.5, 0.5, 1$ and 0, the SM value.

For $c_{HHtt} > 0$, the $HHtt$ diagrams interfere with the box diagrams destructively, which explains the dip in the distribution of $P_{T,H}$ and m_{HH} . We can see a significant depletion in the signal for $c_{HHtt} = 1$, and the destructive interference further depletes the signal for $c_{HHtt} = 0.5$. Peaks for $P_{T,H}$ and m_{HH} stay the same as SM expectations, $P_{T,H} \gtrsim 150$ and $m_{HH} \gtrsim 420$. For $c_{HHtt} < 0$, the differential cross-sections for all observables are enhanced due to the constructive interference between the $HHtt$ diagram and the box diagram. The enhancement is large even when c_{HHtt} is just -0.5 . For y_{HH} and η_H distribution, the overall shape is the same for different values of the $HHtt$ coupling.

By using the parameterization introduced in Eq. (20), the total cross-section of Higgs

FIG. 20. Distributions of $P_{T,H}$, η_H , m_{HH} and y_{HH} for $c_{3H} = 0.5, 1, 2.5, -1$.FIG. 21. Distributions of $P_{T,H}$, η_H , m_{HH} and y_{HH} with $c_{HHtt} = 1, 0.5, 0, -0.5$.

pair production can be written as

$$\begin{aligned} \sigma = \sigma^{SM} [& c_{3H}^2 |\mathcal{M}_{3H}|^2 + c_{Htt}^2 |\mathcal{M}_{Htt}|^2 + c_{HHtt}^2 |\mathcal{M}_{HHtt}|^2 + c_{HWW}^2 |\mathcal{M}_{HWW}|^2 \\ & + c_{HZZ}^2 |\mathcal{M}_{HZZ}|^2 + c_{HWW,Htt}^2 |\mathcal{M}_{HWW,Htt}|^2 + c_{Hbb}^2 |\mathcal{M}_{Hbb}|^2 + c_{Hcc}^2 |\mathcal{M}_{Hcc}|^2 \\ & + 2 c_{3H} c_{Htt} |\mathcal{M}_{3H} \mathcal{M}_{Htt}| + 2 c_{3H} c_{HHtt} |\mathcal{M}_{3H} \mathcal{M}_{HHtt}| + 2 c_{3H} c_{HWW} |\mathcal{M}_{3H} \mathcal{M}_{HWW}| \\ & + 2 c_{3H} c_{HZZ} |\mathcal{M}_{3H} \mathcal{M}_{HZZ}| + 2 c_{3H} c_{HWW,Htt} |\mathcal{M}_{3H} \mathcal{M}_{HWW,Htt}| \\ & + 2 c_{3H} c_{Hbb} |\mathcal{M}_{3H} \mathcal{M}_{Hbb}| + 2 c_{3H} c_{Hcc} |\mathcal{M}_{3H} \mathcal{M}_{Hcc}| \\ & + 2 c_{Htt} c_{HHtt} |\mathcal{M}_{Htt} \mathcal{M}_{HHtt}| + 2 c_{Htt} c_{HWW} |\mathcal{M}_{Htt} \mathcal{M}_{HWW}| + \dots \end{aligned} \quad (22)$$

This expression is lengthy and hard to analyze the effect of changing parameters. Fortunately, \mathcal{M}_{HWW} , \mathcal{M}_{HZZ} , $\mathcal{M}_{HWW,Htt}$, \mathcal{M}_{Hbb} and \mathcal{M}_{Hcc} are very small compare to \mathcal{M}_{3H} , \mathcal{M}_{Htt} and \mathcal{M}_{HHtt} since they comes from QCD_1 contributions. We can therefore safely drop these terms without change the overall properties, and we can write the total cross-section in the following form

$$\begin{aligned} \sigma = \sigma^{SM} [& c_{3H}^2 |\mathcal{M}_{3H}|^2 + c_{Htt}^2 |\mathcal{M}_{Htt}|^2 + c_{HHtt}^2 |\mathcal{M}_{HHtt}|^2 + 2 c_{3H} c_{Htt} |\mathcal{M}_{3H} \mathcal{M}_{Htt}| \\ & + 2 c_{3H} c_{HHtt} |\mathcal{M}_{3H} \mathcal{M}_{HHtt}| + 2 c_{Htt} c_{HHtt} |\mathcal{M}_{Htt} \mathcal{M}_{HHtt}| \end{aligned} \quad (23)$$

For all contributions to the Higgs pair production including $gg \rightarrow HH$, $gg \rightarrow HHg$, $qg \rightarrow HHq$ and $q\bar{q} \rightarrow HHg$, we have

$$\begin{aligned} \sigma = \sigma^{SM} [& 1.8590 c_{Htt}^2 + 0.21485 c_{3H}^2 + 2.9524 c_{HHtt}^2 - 1.0739 c_{Htt} c_{3H} \\ & - 4.1431 c_{Htt} c_{HHtt} + 1.2271 c_{3H} c_{HHtt}]. \end{aligned} \quad (24)$$

A similar result for the LO $gg \rightarrow HH$ at $\sqrt{s} = 100$ is calculated in Ref. 83. For the LHC with $\sqrt{s} = 14$, similar numerical coefficients are found. We stress that the coefficient of c_{3H}^2 is around one order of magnitude lower than those of c_{Htt}^2 and c_{HHtt}^2 , which agrees with the observation made in Ref. 57. Fig. 22 visualize Eq. (24) by showing new physics effects in the total rate of Higgs pair production to the SM expectation ratio. Recently, the upper bound of the Higgs pair production rate was set to 4.1 times the SM value⁸⁰. In the following discussion, the parameters are allowed to vary between -3 and 3 for c_{Htt} and c_{HHtt} , while c_{3H} is allowed to vary between -8 and 8 . In Fig. 22(a), c_{Htt} is fixed to unity, its SM value, while c_{HHtt} is allowed to vary. The green region shows the resulting total rate variation, and a strong enhancement can be found on all allowed regions. When $c_{3H} \lesssim -1.5$ or $c_{3H} \gtrsim 4.1$, the production rate is always enhanced. The red dash-dotted, blue-dashed, and black-solid curves represent three reference cases in the plot for $c_{HHtt} = -1$, $c_{HHtt} = 0$, and $c_{HHtt} = 1$, respectively. The yellow band shows where c_{HHtt} is within ± 0.1 of its expected SM value. Even with vanishing or negative, opposite sign to the SM expectation, trilinear Higgs boson coupling, we can see a large area of the parameter space in c_{Htt} and c_{3H} , which reproduce the same cross-section of the Higgs pair production as in the SM. For the case that c_{HHtt} and c_{Htt} are both close to their SM value, the small area around two intersections of the yellow band and the gray dashed line indicates two possible regions of parameter space that allows c_{3H} to produce the expected SM cross-section value. We can set the allowed limit for SM parameter c_{3H} by finding where the SM curve, blue-dashed curve, reaches the observed limit of production cross-section, 4.1 times the Standard Model prediction. Our result agrees with the finding of⁸⁰, $-1.5 < c_{3H}^{SM} < 6.7$, and we can easily see that c_{HHtt} parameter greatly expand the allowed limit of c_{3H} to $-5 < c_{3H} < 8$. In Fig. 22(b), c_{Htt} is still fixed to unity, but with c_{HHtt} along the horizontal axis. The production cross-section is always enhanced when $c_{HHtt} \lesssim -0.4$ or $c_{HHtt} \gtrsim 1.1$. The yellow band for c_{3H} within ± 0.1 of its expected SM value is very narrow due to the fact that c_{3H} contribution is very small compare to c_{Htt} and c_{HHtt} contributions when $c_{3H} = 1$ (See Fig. 18). Again, two possible regions of parameter space allow c_{HHtt} to produce the expected SM cross-section value when c_{3H} and c_{Htt} are both close to their SM value.

In Fig. 22(c), we fix c_{HHtt} to be its SM value, zero, and c_{Htt} and c_{3H} are both allowed to vary. The black-solid curve in Fig. 22(c) is for the SM c_{Htt} that corresponds to the blue-dashed curve in Fig. 22(a). The minimum σ/σ^{SM} ratio occurs at $c_{3H} \lesssim 2.5$ and has a value

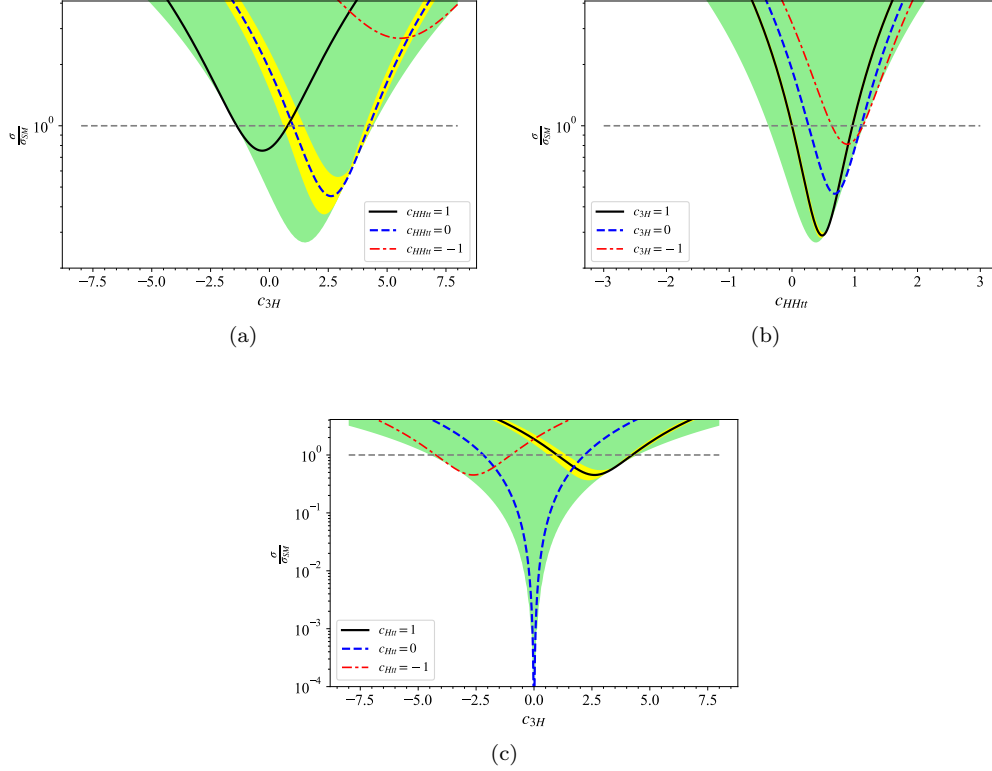


FIG. 22. (a) The ratio of σ/σ^{SM} , with varying c_{HHtt} and c_{3H} while fixing c_{Htt} at unity, are shown as the green region. The yellow band denotes the region where c_{HHtt} is within ± 0.1 of its expected SM value. c_{HHtt} is allowed to vary from -3 to 3 and c_{3H} is allowed to vary from -8 to 8. The SM rate is the dashed horizontal line. (b) Same as (a), but with c_{HHtt} along the horizontal axis. (c) $c_{HHtt} = 0$ with c_{Htt} and c_{3H} varying from -3 to 3 and -8 to 8 respectively. The yellow band denotes the region where c_{Htt} is within ± 0.1 of its expected SM value.

around 0.45, which agrees with the finding of²¹. Notice that zero production cross-section can only occur trivially when three parameters are all zero, and it becomes a minimum point when we vary c_{HHtt} since each contribution can not cancel each other at every phase space point, as we can see in Fig. 20. The SM total rate for the Higgs pair production could be again reproduced by a large area of the parameter space in c_{3H} and c_{Htt} .

We have discussed that it is possible to discover the Higgs pair production in a 100 TeV proton-proton collider which was already shown in Ref. 23, 24, and 56. Then, we study how the event selections affect the extraction of new physics effects in the Higgs pair production. In what follows, the event selections listed in Table III was imposed again. For the signal analysis, full simulations are performed for parameters within the range $-3 < c_{3H, Htt, HHtt} < 3$. Then, as the partonic case, we can fit the number of selected signal events by a similar function shown in Eq. (24). The contributions of different diagrams would cause different selection efficiency due to the fact that the kinematic distributions are different for each diagram. However, we can still factor out the parameters c_{Htt} , c_{3H} and c_{HHtt} during the calculations, and this will again give a simple parameterization:

$$\sigma = \sigma^{SM} [3.1265 c_{HHtt}^2 + 1.5332 c_{Htt}^2 + 0.072904 c_{3H}^2 - 3.7322 c_{Htt} c_{HHtt} - 0.60614 c_{3H} c_{HHtt} + 0.81739 c_{3H} c_{Htt}]. \quad (25)$$

In Fig. 23, we consider constraints on c_{Htt} , c_{3H} and c_{HHtt} from measurements of the total cross-section at CM energy of 100 TeV with contour lines go along 25% and 50% deviations

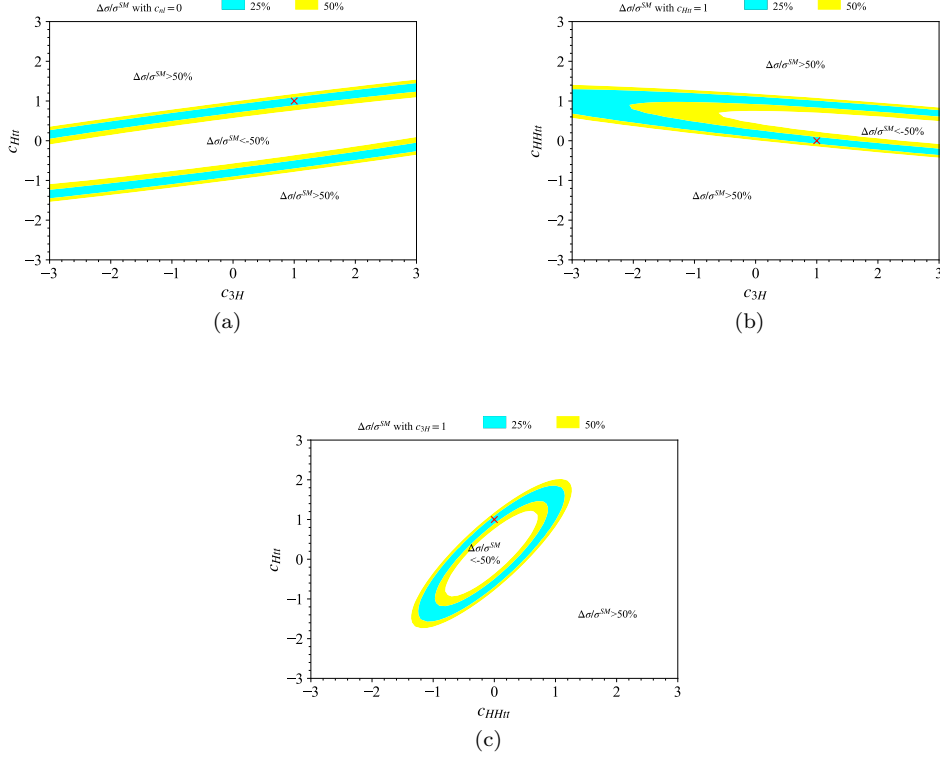


FIG. 23. Cross-section contour plot for $gg \rightarrow hh \rightarrow \gamma\gamma b\bar{b}$ channel after including the veto cuts in Table III. The parameter space that match the expected SM values within 25% and 50% are indicated by cyan and yellow areas, respectively. The red cross marks the SM value.

from the SM value. For each plot in Fig. 23, we vary two of c_{3H} , c_{Htt} and c_{HHtt} and fix the rest to the SM value. For example, in Fig. 23(a), c_{Htt} and c_{3H} are allowed to vary within the interval $(-3, 3)$, while $c_{HHtt} = 0$ as in the SM.

The cyan and yellow bands represent the parameter spaces that match the result of SM within 25% and 50%, respectively. We see that the sensitivity of cross-section to c_{3H} is low. The same insensitivity remains in Fig. 23(b), where we set c_{Htt} to unity, its SM value.

In Fig. 23(c), where $c_{3H} = 1$ takes the SM value and c_{Htt} , c_{HHtt} are varying within the interval $(-3, 3)$. Moreover, due to the fact that the triangle diagrams interfere with box diagrams destructively, increasing c_{HHtt} can offset any effect of increasing c_{Htt} . Therefore, to explain the various contributions of new physics in double Higgs production, total cross-section alone is not sufficient, and further studies for additional kinematic information are needed.

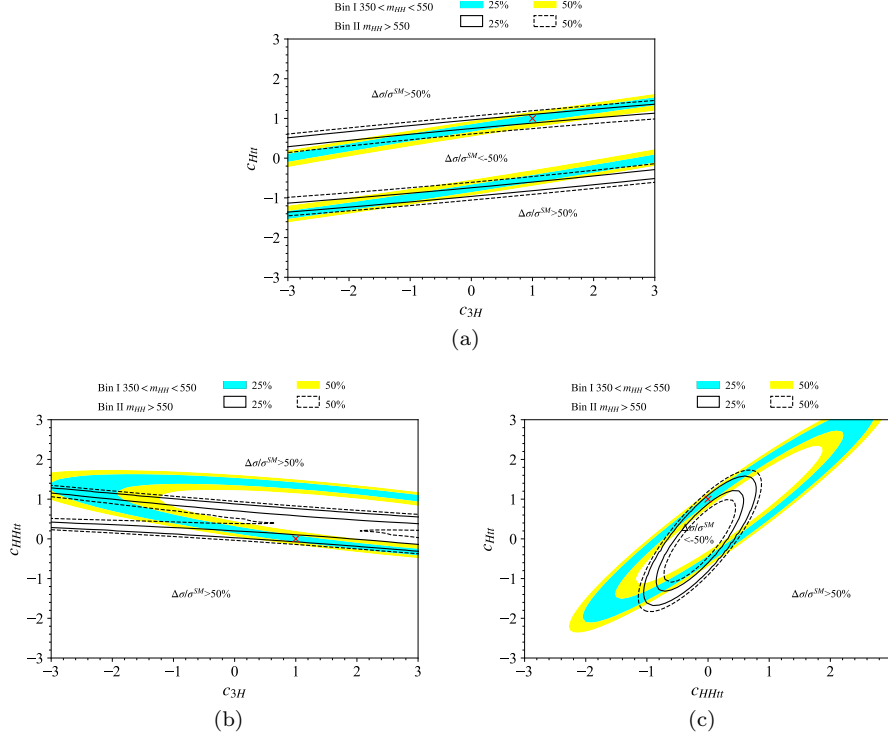


FIG. 24. Contour plots for the cross-sections of a high energy and a low energy bin. Bin I: $350 \text{ GeV} < m_{HH} < 550 \text{ GeV}$ and Bin II: $m_{HH} > 550 \text{ GeV}$. The cross-section matching the value of SM within 25% is shown as the cyan region for Bin I and the region between two solid-black curves for Bin II. The cross-section that is within 25 – 50% of SM expectation is shown as the yellow region for Bin I and the region between solid and dashed curves for Bin II. The red cross mark the SM value.

As we have already seen, the contributions of c_{Htt} , c_{3H} and c_{HHtt} have very different distributions of p_T^h and m_{HH} . The c_{3H} component peaks at low m_{HH} , the c_{Htt} peaks at a higher m_{HH} , and the c_{HHtt} shifts the m_{HH} distribution to even larger values. (See Fig. 18). Following the analysis in Ref. 83, we divide the m_{HH} and p_T distributions into a low bin and a high bin, and the differential cross-section in each bin is used to constrain c_{Htt} , c_{3H} , and c_{HHtt} . We note that fitting the two p_T bins and the two m_{HH} bins give quite similar constraints, which are consistent with the results of⁸³. Therefore, in the following, we only show the contour plots of the constraints from fitting the two m_{HH} bins. From Fig. 17, the following two m_{HH} bins are chosen in our analysis.

$$\text{Bin I : } 350 \text{ GeV} \leq m_{HH} \leq 550 \text{ GeV}$$

$$\text{Bin II : } 550 \text{ GeV} \leq m_{HH}$$

For Bin I and Bin II, the parameterizations of the cross-sections with respect to c_{Htt} , c_{3H} and c_{HHtt} are given in Eq. (25).

$$\begin{aligned} \sigma_I &= \sigma_I^{SM} [2.1837 c_{HHtt}^2 + 1.6984 c_{Htt}^2 + 0.10647 c_{3H}^2 - 3.6533 c_{Htt} c_{HHtt} \\ &\quad - 0.80491 c_{3H} c_{HHtt} + 0.71334 c_{3H} c_{Htt}]. \\ \sigma_{II} &= \sigma_{II}^{SM} [4.2030 c_{HHtt}^2 + 1.3446 c_{Htt}^2 + 0.03458 c_{3H}^2 - 3.8224 c_{Htt} c_{HHtt} \\ &\quad - 0.37915 c_{3H} c_{HHtt} + 0.93621 c_{3H} c_{Htt}]. \end{aligned} \quad (26)$$

Fig. 24 shows the constraints from the differential cross-section, which lie within 25% and 50% of SM expectations in each bin. Again, two of c_{Htt} , c_{3H} , and c_{HHtt} are allowed to vary, while the other is fixed at the SM value. In Fig. 24(a), where c_{HHtt} is fixed while c_{3H}

and c_{Htt} are allowed to vary, this set of contours has the largest overlap among all three sets of contours. In Fig. 24(b), where $c_{3H} = 1$, we see only a small overlap between the contour from Bin I and Bin II, and the degeneracies in c_{3H} and c_{HHtt} are broken effectively by the measurements in the two bins. In Fig. 24(c), where c_{Htt} is allowed to vary, along with c_{HHtt} , we see the non-overlapping region becomes larger than in Fig. 24(b). However, the change of c_{Htt} from its SM value is expected to be small due to the precise weak interaction measurements already done. Therefore, the relation present in Fig. 24(c) may not be as useful as in Fig. 24(b). Our results shown in Fig. 24(a) and Fig. 24(c) are similar to the finding of⁸³ by using LO with Higgs effective theory corrections to calculate the cross-section. For the contour shown in Fig. 24(b), on the other hand, we have a much larger non-overlapping region near SM expectation compare to the finding of⁸³. Therefore full NLO calculations are required due to the effects of event selections on $gg \rightarrow HHg$ and $qg \rightarrow HHq$ channels. Nonetheless, we note that some degeneracy remains when the differential cross-sections in the low and high bins meet the expected SM values. When it comes to constraining c_{3H} , the situation worsens. However, a significant improvement in constraining c_{3H} from using the measurement of total cross-section alone can still be achieved by including the kinematic information from both low and high m_{HH} bins.

VII. CONCLUSION

In this work, we investigated the use of the kinematic distribution to reveal the new physics effects in the Higgs pair production, including LO channel, $gg \rightarrow HH$, and all NLO channels, $gg \rightarrow HHg$, $qg \rightarrow HHq$, and $qq \rightarrow HHg$. We showed that three dimensionless coefficients, c_{Htt} , c_{3H} , and c_{HHtt} , can be used to parameterize the differential cross-section with various new physics effects. We investigated the interactions of different contributions in the p_T spectra and the invariant mass spectra of the Higgs pair. We then numerically study the constraints of these parameters in a 100 TeV proton-proton collider under planning by finding the best fit for the differential rates in a low and a high m_{HH} as well as p_T bins. The constraints from low and high bins ended up being very similar to those from the two p_T bins. Finally, it was found that we can constrain c_{Htt} and c_{HHtt} effectively, despite some degeneracy persists. Moreover, the coefficient c_{3H} , which directly reveals the effect of trilinear Higgs self-coupling, is less constrained. This is roughly consistent with the earlier result in the LO $gg \rightarrow HH$ channel⁸³, full NLO calculations that more effectively break the degeneracy in c_{3H} and c_{HHtt} are therefore required.

Nonetheless, the extra kinematic information from the two invariant mass bins still gives much better results than the total cross-section alone.

Measurements of the trilinear Higgs coupling should be a top priority in upcoming research programs on the Higgs boson, since only the properties of Higgs self-interaction of the 125 GeV Higgs boson have not been thoroughly tested experimentally. Recent searches⁸⁰ for pairs of Higgs bosons in $HH \rightarrow \gamma\gamma b\bar{b}$ process set a limit on the double Higgs production rate of 4.1 times the SM value and created a portal to better understanding the fundamental Higgs mechanism.

The work is far from done. Much more work needs to be done in the phenomenology of double Higgs production. The Matrix Element Method based multivariate analysis⁸⁴, which has been applied to the Higgs discovery in the 4ℓ channel^{85–90} and the top quark analyses^{91–95} can be performed to exploit the full kinematic information in the future. Also, the recent search for the Higgs pair performed by the ATLAS collaboration, which applied multivariate analysis based on Boosted Decision Trees (BDT) to event selection in the SM process, obtained the best limit for the double Higgs boson production currently. The same technique can be applied to searches for new physics in the future.

¹G. Aad *et al.*, “Observation of a new particle in the search for the Standard Model Higgs boson with the ATLAS detector at the LHC,” *Phys. Lett. Sect. B Nucl. Elem. Part. High-Energy Phys.* **716**, 1–29 (2012), arXiv:1207.7214.

²S. Chatrchyan *et al.*, “Observation of a new boson at a mass of 125 GeV with the CMS experiment at the LHC,” *Phys. Lett. Sect. B Nucl. Elem. Part. High-Energy Phys.* **716**, 30–61 (2012), arXiv:1207.7235.

- ³A. collaboration, “Measurements of the Higgs boson production and decay rates and constraints on its couplings from a combined ATLAS and CMS analysis of the LHC pp collision data at $\sqrt{s} = 7$ and 8 TeV,” *J. High Energy Phys.* **2016** (2016), 10.1007/JHEP08(2016)045, arXiv:1606.02266.
- ⁴P. W. Higgs, “Broken symmetries, massless particles and gauge fields,” *Phys. Lett.* **12**, 132–133 (1964).
- ⁵P. W. Higgs, “Broken symmetries and the masses of gauge bosons,” *Phys. Rev. Lett.* **13**, 508–509 (1964).
- ⁶P. W. Higgs, “Spontaneous symmetry breakdown without massless bosons,” *Phys. Rev.* **145**, 1156–1163 (1966).
- ⁷F. Englert and R. Brout, “Broken symmetry and the mass of gauge vector mesons,” *Phys. Rev. Lett.* **13**, 321–323 (1964).
- ⁸G. S. Guralnik, C. R. Hagen, and T. W. Kibble, “Global conservation laws and massless particles,” *Phys. Rev. Lett.* **13**, 585–587 (1964).
- ⁹T. W. Kibble, “Symmetry breaking in n-Abelian gauge theories,” *Phys. Rev.* **155**, 1554–1561 (1967).
- ¹⁰ATLAS Collaboration, “Update of the Combination of Higgs Boson Searches in 1.0 to 2.3 fb⁻¹ of *pp* Collisions Data Taken at $\sqrt{s} = 7$ TeV with the ATLAS Experiment at the LHC,” Cern. Geneva Switz. (2011).
- ¹¹C. collaboration, “Combined results of searches for a Higgs boson in the context of the standard model and beyond-standard models,” *Hig-12-008* **600** (2012).
- ¹²C. Anastasiou, R. Boughezal, and E. Furlan, “The NNLO gluon fusion Higgs production cross-section with many heavy quarks,” *J. High Energy Phys.* **2010** (2010), 10.1007/JHEP06(2010)101, arXiv:1003.4677.
- ¹³C. Anastasiou, S. Buehler, E. Furlan, F. Herzog, and A. Lazopoulos, “Higgs production cross-section in a Standard Model with four generations at the LHC,” *Phys. Lett. Sect. B Nucl. Elem. Part. High-Energy Phys.* **702**, 224–227 (2011), arXiv:1103.3645.
- ¹⁴A. Djouadi and A. Lenz, “Sealing the fate of a fourth generation of fermions,” *Phys. Lett. Sect. B Nucl. Elem. Part. High-Energy Phys.* **715**, 310–314 (2012), arXiv:1204.1252.
- ¹⁵A. Denner, S. Dittmaier, A. Mück, G. Passarino, M. Spira, C. Sturm, S. Uccirati, and M. M. Weber, “Higgs production and decay with a fourth Standard-Model-like fermion generation,” *Eur. Phys. J. C* **72**, 1–15 (2012), arXiv:1111.6395.
- ¹⁶O. Eberhardt, G. Herbert, H. Lacker, A. Lenz, A. Menzel, U. Nierste, and M. Wiebusch, “Impact of a Higgs boson at a mass of 126 GeV on the standard model with three and four fermion generations,” *Phys. Rev. Lett.* **109** (2012), 10.1103/PhysRevLett.109.241802, arXiv:1209.1101.
- ¹⁷V. Khachatryan *et al.*, “Precise determination of the mass of the Higgs boson and tests of compatibility of its couplings with the standard model predictions using proton collisions at 7 and 8 TeV,” *Eur. Phys. J. C* **75** (2015), 10.1140/epjc/s10052-015-3351-7, arXiv:1412.8662.
- ¹⁸ATLAS Collaboration, “Combined measurements of the Higgs boson production and decay rates in $H \rightarrow ZZ^* \rightarrow 4\ell$ and $H \rightarrow \gamma\gamma$ final states using *pp* collision data at $\sqrt{s} = 13$ TeV in the ATLAS experiment,” ATLAS-CONF-2016-081 (2016).
- ¹⁹G. Degrandi, P. Giardino, F. Maltoni, and D. Pagani, “Probing the Higgs self coupling via single Higgs production at the LHC,” *J. High Energy Phys.* **2016**, 80 (2016).
- ²⁰G. Degrandi, M. Fedele, and P. Giardino, “Constraints on the trilinear Higgs self coupling from precision observables,” *J. High Energy Phys.* **2017**, 155 (2017).
- ²¹J. Baglio, F. Campanario, S. Glaus, M. Mühlleitner, J. Ronca, M. Spira, and J. Streicher, “Higgs-pair production via gluon fusion at hadron colliders: NLO QCD corrections,” *J. High Energy Phys.* **2020** (2020), 10.1007/JHEP04(2020)181.
- ²²X. Li and M. B. Voloshin, “Remarks on double Higgs boson production by gluon fusion at threshold,” *Phys. Rev. D - Part. Fields, Gravit. Cosmol.* **89** (2014), 10.1103/PhysRevD.89.013012, arXiv:1311.5156.
- ²³J. Baglio, A. Djouadi, R. Gröber, M. M. Mühlleitner, J. Quevillon, and M. Spira, “The measurement of the Higgs self-coupling at the LHC: Theoretical status,” *J. High Energy Phys.* **2013** (2013), 10.1007/JHEP04(2013)151, arXiv:1212.5581.
- ²⁴W. Yao, “Studies of measuring Higgs self-coupling with $HH \rightarrow b\bar{b}\gamma\gamma$ at the future hadron colliders,” **1**, 8 (2013), arXiv:1308.6302.
- ²⁵O. J. Éboli, G. C. Marques, S. F. Novaes, and A. A. Natale, “Twin Higgs-boson production,” *Phys. Lett. B* **197**, 269–272 (1987).
- ²⁶E. W. Glover and J. J. van der Bij, “Higgs boson pair production via gluon fusion,” *Nucl. Physics, Sect. B* **309**, 282–294 (1988).
- ²⁷D. A. Dicus, C. Kao, and S. S. Willenbrock, “Higgs boson pair production from gluon fusion,” *Phys. Lett. B* **203**, 457–461 (1988).
- ²⁸T. Plehn, M. Spira, and P. M. Zerwas, “Pair production of neutral Higgs particles in gluon-gluon collisions,” *Nucl. Phys. B* **479**, 46–64 (1996), arXiv:9603205 [hep-ph].
- ²⁹A. Dobrovolskaya and V. Novikov, “On heavy Higgs boson production,” *Zeitschrift für Phys. C Part. Fields* **52**, 427–436 (1991).
- ³⁰D. A. Dicus, K. J. Kallianpur, and S. S. Willenbrock, “Higgs boson pair production in the effective-W approximation,” *Phys. Lett. B* **200**, 187–192 (1988).
- ³¹W.-Y. Keung, “DOUBLE HIGGS FROM W-W FUSION,” *Mod. Phys. Lett. A* **02**, 765–770 (1987).
- ³²A. Abbasabadi, W. W. Repko, D. A. Dicus, and R. Vega, “Comparison of exact and effective-gauge-boson calculations for gauge-boson fusion processes,” *Phys. Rev. D* **38**, 2770–2775 (1988).
- ³³V. Barger, T. Han, and R. J. Phillips, “Double Higgs-boson bremsstrahlung from W and Z bosons at supercolliders,” *Phys. Rev. D* **38**, 2766–2769 (1988).

- ³⁴M. Moretti, S. Moretti, F. Piccinini, R. Pittau, and A. D. Polosa, “Higgs boson self-couplings at the LHC as a probe of extended Higgs sectors,” *J. High Energy Phys.* **2005**, 603–619 (2005).
- ³⁵T. Plehn and M. Rauch, “Quartic Higgs coupling at hadron colliders,” *Phys. Rev. D* **72**, 053008 (2005).
- ³⁶T. Binoth, S. Karg, N. Kauer, and R. Rückl, “Multi-Higgs boson production in the standard model and beyond,” *Phys. Rev. D* **74**, 113008 (2006).
- ³⁷B. Fuks, J. H. Kim, and S. J. Lee, “Probing Higgs boson self-interactions in proton-proton collisions at a center-of-mass energy of 100 TeV,” *Phys. Rev. D* **93**, 035026 (2016).
- ³⁸D. de Florian and J. Mazzitelli, “Two-loop corrections to the triple Higgs boson production cross section,” *J. High Energy Phys.* **2017**, 107 (2017).
- ³⁹D. de Florian, I. Fabre, and J. Mazzitelli, “Triple Higgs production at hadron colliders at NNLO in QCD,” *J. High Energy Phys.* **2020** (2020), 10.1007/JHEP03(2020)155, arXiv:1912.02760.
- ⁴⁰The quartic Higgs coupling is indirectly constrained by Higgs pair production ^{96–98}.
- ⁴¹S. Borowka, N. Greiner, G. Heinrich, S. P. Jones, M. Kerner, J. Schlenk, U. Schubert, and T. Zirke, “Higgs Boson Pair Production in Gluon Fusion at Next-to-Leading Order with Full Top-Quark Mass Dependence [Phys. Rev. Lett. 117, 012001 (2016)],” *Phys. Rev. Lett.* **117**, 079901 (2016).
- ⁴²S. Borowka, N. Greiner, G. Heinrich, S. Jones, M. Kerner, J. Schlenk, and T. Zirke, “Full top quark mass dependence in Higgs boson pair production at NLO,” *J. High Energy Phys.* **2016**, 107 (2016).
- ⁴³J. Baglio, F. Campanario, S. Glaus, M. Mühlleitner, M. Spira, and J. Streicher, “Gluon fusion into Higgs pairs at NLO QCD and the top mass scheme,” *Eur. Phys. J. C* **79**, 459 (2019).
- ⁴⁴D. de Florian and J. Mazzitelli, “Two-loop virtual corrections to Higgs pair production,” *Phys. Lett. B* **724**, 306–309 (2013).
- ⁴⁵D. de Florian and J. Mazzitelli, “Higgs Boson Pair Production at Next-to-Next-to-Leading Order in QCD,” *Phys. Rev. Lett.* **111**, 201801 (2013).
- ⁴⁶J. Grigo, K. Melnikov, and M. Steinhauser, “Virtual corrections to Higgs boson pair production in the large top quark mass limit,” *Nucl. Phys. B* **888**, 17–29 (2014), arXiv:1408.2422.
- ⁴⁷M. Spira, “Effective multi-Higgs couplings to gluons,” *J. High Energy Phys.* **2016** (2016), 10.1007/JHEP10(2016)026, arXiv:1607.05548.
- ⁴⁸P. Banerjee, S. Borowka, P. K. Dhani, T. Gehrmann, and V. Ravindran, “Two-loop massless QCD corrections to the $g + g \rightarrow H + H$ four-point amplitude,” *J. High Energy Phys.* **2018**, 130 (2018).
- ⁴⁹L. B. Chen, H. T. Li, H. S. Shao, and J. Wang, “Higgs boson pair production via gluon fusion at N3LO in QCD,” *Phys. Lett. Sect. B Nucl. Elem. Part. High-Energy Phys.* **803** (2020), 10.1016/j.physletb.2020.135292, arXiv:1909.06808.
- ⁵⁰L. B. Chen, H. T. Li, H. S. Shao, and J. Wang, “The gluon-fusion production of Higgs boson pair: N3LO QCD corrections and top-quark mass effects,” *J. High Energy Phys.* **2020** (2020), 10.1007/JHEP03(2020)072, arXiv:1912.13001.
- ⁵¹G. Heinrich, S. P. Jones, M. Kerner, G. Luisoni, and E. Vryonidou, “NLO predictions for Higgs boson pair production with full top quark mass dependence matched to parton showers,” *J. High Energy Phys.* **2017** (2017), 10.1007/JHEP08(2017)088, arXiv:1703.09252.
- ⁵²S. Jones and S. Kuttimalai, “Parton shower and NLO-matching uncertainties in Higgs boson pair production,” *J. High Energy Phys.* **2018** (2018), 10.1007/JHEP02(2018)176, arXiv:1711.03319.
- ⁵³M. Grazzini, G. Heinrich, S. Jones, S. Kallweit, M. Kerner, J. M. Lindert, and J. Mazzitelli, “Higgs boson pair production at NNLO with top quark mass effects,” *J. High Energy Phys.* **2018** (2018), 10.1007/JHEP05(2018)059, arXiv:1803.02463.
- ⁵⁴C. O. Dib, R. Rosenfeld, and A. Zerwekh, “Double Higgs production and quadratic divergence cancellation in little Higgs models with T-parity,” *J. High Energy Phys.* **2006** (2006), 10.1088/1126-6708/2006/05/074, arXiv:0509179 [hep-ph].
- ⁵⁵R. Gröber and M. Mühlleitner, “Composite Higgs boson pair production at the LHC,” *J. High Energy Phys.* **2011** (2011), 10.1007/JHEP06(2011)020, arXiv:1012.1562.
- ⁵⁶H.-J. He, J. Ren, and W. Yao, “Probing New Physics of Cubic Higgs Interaction via Higgs Pair Production at Hadron Colliders,” (2015), 10.1103/PhysRevD.93.015003, arXiv:1506.03302.
- ⁵⁷R. Contino, M. Ghezzi, M. Moretti, G. Panico, F. Piccinini, and A. Wulzer, “Anomalous couplings in double Higgs production,” *J. High Energy Phys.* **2012** (2012), 10.1007/JHEP08(2012)154, arXiv:1205.5444.
- ⁵⁸A. Abada *et al.*, “FCC Physics Opportunities,” *Eur. Phys. J. C* **79**, 474 (2019).
- ⁵⁹A. Abada *et al.*, “FCC-hh: The Hadron Collider,” *Eur. Phys. J. Spec. Top.* **228**, 755–1107 (2019).
- ⁶⁰Comparing the notations in Ref. 83 to our result, we have $c_{3H} = c_{\Delta}$, $c_{Htt} = c_{\square}$, and $c_{HHtt} = c_{nl}$.
- ⁶¹M. Gillioz, R. Gröber, C. Grojean, M. Mühlleitner, and E. Salvioni, “Higgs low-energy theorem (and its corrections) in composite models,” *J. High Energy Phys.* **2012** (2012), 10.1007/JHEP10(2012)004, arXiv:1206.7120.
- ⁶²S. Dawson, E. Furlan, and I. Lewis, “Unravelling an extended quark sector through multiple higgs production?” *Phys. Rev. D - Part. Fields, Gravit. Cosmol.* **87** (2013), 10.1103/PhysRevD.87.014007, arXiv:1210.6663.
- ⁶³J. Ellis, M. K. Gaillard, and D. Nanopoulos, “A phenomenological profile of the Higgs boson,” *Nucl. Phys. B* **106**, 292–340 (1976).
- ⁶⁴T. Hahn, “Generating Feynman diagrams and amplitudes with FeynArts 3,” *Comput. Phys. Commun.* **140**, 418–431 (2001).
- ⁶⁵T. Hahn and M. Pérez-Victoria, “Automated one-loop calculations in four and D dimensions,” *Comput. Phys. Commun.* **118**, 153–165 (1999).

- ⁶⁶G. van Oldenborgh, “FF — a package to evaluate one-loop Feynman diagrams,” *Comput. Phys. Commun.* **66**, 1–15 (1991).
- ⁶⁷A. Denner and S. Dittmaier, “Reduction of one-loop tensor 5-point integrals,” *Nucl. Phys. B* **658**, 175–202 (2003).
- ⁶⁸A. Denner and S. Dittmaier, “Reduction schemes for one-loop tensor integrals,” *Nucl. Phys. B* **734**, 62–115 (2006).
- ⁶⁹A. Denner, S. Dittmaier, and L. Hofer, “Collier: A fortran-based complex one-loop library in extended regularizations,” *Comput. Phys. Commun.* **212**, 220–238 (2017).
- ⁷⁰G. ’t Hooft and M. Veltman, “Scalar one-loop integrals,” *Nucl. Phys. B* **153**, 365–401 (1979).
- ⁷¹R. Frederix, S. Frixione, V. Hirschi, D. Pagani, H. S. Shao, and M. Zaro, “The automation of next-to-leading order electroweak calculations,” *J. High Energy Phys.* **2018** (2018), 10.1007/JHEP07(2018)185, arXiv:1804.10017.
- ⁷²J. Butterworth *et al.*, “PDF4LHC recommendations for LHC Run II,” *J. Phys. G Nucl. Part. Phys.* **43**, 023001 (2016).
- ⁷³T. Sjöstrand, S. Ask, J. R. Christiansen, R. Corke, N. Desai, P. Ilten, S. Mrenna, S. Prestel, C. O. Rasmussen, and P. Z. Skands, “An introduction to PYTHIA 8.2,” *Comput. Phys. Commun.* **191**, 159–177 (2015), arXiv:1410.3012.
- ⁷⁴J. De Favereau, C. Delaere, P. Demin, A. Giammanco, V. Lemaitre, A. Mertens, and M. Selvaggi, “DELPHES 3: A modular framework for fast simulation of a generic collider experiment,” *J. High Energy Phys.* **2014** (2014), 10.1007/JHEP02(2014)057, arXiv:1307.6346.
- ⁷⁵C. Degrande, C. Duhr, B. Fuks, D. Grellscheid, O. Mattelaer, and T. Reiter, “UFO - The Universal FeynRules Output,” *Comput. Phys. Commun.* **183**, 1201–1214 (2012), arXiv:1108.2040.
- ⁷⁶U. Baur, T. Plehn, and D. Rainwater, “Measuring the Higgs boson self-coupling at the large hadron collider,” *Phys. Rev. Lett.* **89**, 151801/1–151801/4 (2002), arXiv:0206024 [hep-ph].
- ⁷⁷U. Baur, T. Plehn, and D. Rainwater, “Determining the Higgs boson self-coupling at hadron colliders,” *Phys. Rev. D - Part. Fields, Gravit. Cosmol.* **67**, 033003 (2003), arXiv:0211224 [hep-ph].
- ⁷⁸U. Baur, T. Plehn, and D. Rainwater, “Examining the Higgs boson potential at lepton and hadron colliders: A comparative analysis,” *Phys. Rev. D* **68**, 033001 (2003).
- ⁷⁹U. Baur, T. Plehn, and D. Rainwater, “Probing the Higgs self-coupling at hadron colliders using rare decays,” *Phys. Rev. D - Part. Fields, Gravit. Cosmol.* **69**, 053004 (2004), arXiv:0310056 [hep-ph].
- ⁸⁰R. Owen and S. R. A. Laboratory, “Higgs physics results at ATLAS on behalf of the ATLAS Collaboration,” *Tech. Rep.* (2021).
- ⁸¹“Performance assumptions for an upgraded ATLAS detector at a High-Luminosity LHC,” (2013).
- ⁸²R. Contino and Others, “Physics at a 100 TeV pp collider: Higgs and EW symmetry breaking studies,” *Cern Yellow Rep.*, 255–440 (2017), arXiv:1606.09408 [hep-ph].
- ⁸³C.-R. Chen and I. Low, “Double take on new physics in double Higgs boson production,” *Phys. Rev. D* **90**, 013018 (2014).
- ⁸⁴K. Kondo, “Dynamical Likelihood Method for Reconstruction of Events with Missing Momentum. I. Method and Toy Models,” *J. Phys. Soc. Japan* **57**, 4126–4140 (1988).
- ⁸⁵S. Chatrchyan *et al.*, “Measurement of the properties of a Higgs boson in the four-lepton final state,” *Phys. Rev. D - Part. Fields, Gravit. Cosmol.* **89** (2014), 10.1103/PhysRevD.89.092007, arXiv:1312.5353.
- ⁸⁶A. De Rújula, J. Lykken, M. Pierini, C. Rogan, and M. Spiropulu, “Higgs boson look-alikes at the LHC,” *Phys. Rev. D - Part. Fields, Gravit. Cosmol.* **82** (2010), 10.1103/PhysRevD.82.013003, arXiv:1001.5300.
- ⁸⁷J. S. Gainer, K. Kumar, I. Low, and R. Vega-Morales, “Improving the sensitivity of Higgs boson searches in the golden channel,” *J. High Energy Phys.* **2011** (2011), 10.1007/JHEP11(2011)027, arXiv:1108.2274.
- ⁸⁸Y. Gao, A. V. Gritsan, Z. Guo, K. Melnikov, M. Schulze, and N. V. Tran, “Spin determination of single-produced resonances at hadron colliders,” *Phys. Rev. D - Part. Fields, Gravit. Cosmol.* **81** (2010), 10.1103/PhysRevD.81.075022, arXiv:1001.3396.
- ⁸⁹S. Chatrchyan *et al.*, “Study of the mass and spin-parity of the Higgs boson candidate via its decays to Z boson pairs,” *Phys. Rev. Lett.* **110** (2013), 10.1103/PhysRevLett.110.081803, arXiv:1212.6639.
- ⁹⁰S. Chatrchyan *et al.*, “Observation of a new boson with mass near 125 GeV in pp collisions at $\sqrt{s} = 7$ and 8 TeV,” *J. High Energy Phys.* **2013** (2013), 10.1007/JHEP06(2013)081, arXiv:1303.4571.
- ⁹¹R. H. Dalitz and G. R. Goldstein, “Decay and polarization properties of the top quark,” *Phys. Rev. D* **45**, 1531–1543 (1992).
- ⁹²B. Abbott *et al.*, “Measurement of the top quark mass in the dilepton channel,” *Phys. Rev. D - Part. Fields, Gravit. Cosmol.* **60** (1999), 10.1103/PhysRevD.60.052001, arXiv:9808029 [hep-ex].
- ⁹³T. Aaltonen *et al.*, “Measurement of the single-top-quark production cross section at CDF,” *Phys. Rev. Lett.* **101** (2008), 10.1103/PhysRevLett.101.252001, arXiv:0809.2581.
- ⁹⁴A. Abulencia *et al.*, “Top quark mass measurement from dilepton events at CDF II with the matrix-element method,” *Phys. Rev. D - Part. Fields, Gravit. Cosmol.* **74** (2006), 10.1103/PhysRevD.74.032009, arXiv:0605118 [hep-ex].
- ⁹⁵V. M. Abazov *et al.*, “Evidence for production of single top quarks,” *Phys. Rev. D - Part. Fields, Gravit. Cosmol.* **78** (2008), 10.1103/PhysRevD.78.012005, arXiv:0803.0739.
- ⁹⁶T. Liu, K.-F. Lyu, J. Ren, and H. X. Zhu, “Probing the quartic Higgs boson self-interaction,” *Phys. Rev. D* **98**, 093004 (2018).
- ⁹⁷W. Bizoń, U. Haisch, and L. Rottoli, “Constraints on the quartic Higgs self-coupling from double-Higgs production at future hadron colliders,” *J. High Energy Phys.* **2019**, 267 (2019).

- ⁹⁸S. Borowka, C. Duhr, F. Maltoni, D. Pagani, A. Shivaji, and X. Zhao, “Probing the scalar potential via double Higgs boson production at hadron colliders,” *J. High Energy Phys.* **2019**, 16 (2019).